공학석사 학위논문

Study on the Effect of Mn Structure and Valency on Water Oxidation Catalysis

- New Manganese Phosphate Crystal and Lithium Manganese Pyrophosphate with tunable Mn valency as Water Oxidation Catalysts -

망간의 구조와 산화수가 산소 발생 촉매 작용에 미치는 영향에 대한 연구

2014년 2월

서울대학교 대학원

재료공학부

박 지 민

Study on the Effect of Mn Structure and Valency on Water Oxidation Catalysis

- New Manganese Phosphate Crystal and Lithium Manganese Pyrophosphate with tunable Mn valency as Water Oxidation Catalysts -

지도 교수 남 기 태

이 논문을 공학석사 학위논문으로 제출함

2014 년 2 월

서울대학교 대학원

재료공학부

박 지 민

박지민의 석사 학위논문을 인준함

2014 년 2 월

위 원 장	한 승 우	(인)
부위원장	남 기 태	(인)
위 원	강 기 석	(인)

Abstract

Study on the Effect of Mn Structure and Valency on Water Oxidation Catalysis

Jimin Park
Department of Materials Science and Engineering
The Graduate School
Seoul National University

The development of a water oxidation catalyst has been a demanding challenge for the realization of overall water-splitting systems. The asymmetric geometry and flexible ligation of the biological Mn_4CaO_5 cluster are important properties for the function of photosystem II, and these properties can be applied to the design of a new inorganic water oxidation catalyst. In part I, we identified a new crystal structure, $Mn_3(PO_4)_2$-$3H_2O$, that precipitates spontaneously in aqueous solution at room temperature and demonstrated its superior catalytic performance at neutral pH. Computational analysis indicated that phosphate ligations in our crystal make Mn-O bonding longer and more distorted than in other Mn-based oxides. Such structural flexibility can stabilize Jahn-Teller distorted Mn(III) and thus facilitate Mn(II) oxidation, as monitored by electron paramagnetic resonance spectroscopy.

Moreover, although intensive studies have explored the role of Mn

element in water oxidation catalysis, it has been difficult to understand whether the catalytic capability originates mainly from either the Mn arrangement or the Mn valency. In part II, to decouple these two factors and to investigate the role of Mn valency on catalysis, we selected a new pyrophosphate-based Mn compound ($Li_2MnP_2O_7$), which has not been utilized for water oxidation catalysis to date, as a model system. Due to the monophasic behavior of $Li_2MnP_2O_7$ with the delithiation, the Mn valency of $Li_{2-x}MnP_2O_7$ (x = 0.3, 0.5, 1) can be controlled with negligible change in crystal framework (e.g. volume change ~ 1 %). Interestingly, we observed that as the averaged oxidation state of Mn in $Li_{2-x}MnP_2O_7$ increases from 2 to 3, the catalytic performance is enhanced in the series $Li_2MnP_2O_7$ < $Li_{1.7}MnP_2O_7$ < $Li_{1.5}MnP_2O_7$ < $LiMnP_2O_7$. Moreover, $Li_2MnP_2O_7$ itself exhibits superior catalytic performance compared with MnO or MnO_2 because of the highly distorted Mn geometry in $Li_2MnP_2O_7$.

In summary, we selected $Mn_3(PO_4)_2$-$3H_2O$ and $Li_{2-x}MnP_2O_7$ compounds as artificial platforms for understanding the effect of Mn structure and valency on water oxidation catalysis, respectively. We think that this study presents valuable guidelines for developing an efficient Mn-based catalyst which can be comparable with the biological Mn_4CaO_5 cluster in photosystem II under neutral conditions with controlled Mn valency and atomic arrangement.

Keywords: water splitting, oxygen evolution reaction, $Mn_3(PO_4)_2$-$3H_2O$, $Li_2MnP_2O_7$, Neutral condition, Mn structure and valency

Student Number: 2012-20600

Contents

List of Tables

List of Figures

Chapter 1. Introduction

1.1 Energy Crisis and Demand for renewable energy

During the 20th century, energy supplies mainly from fossil fuels have offered opportunities to generate electricity and heat which buttressed the human-lives.[1] As human-lives have progressed, high demand of energy has been required, and consequently the consumption of fossil fuels has increased to 2 liters a day for each person on the world.[1] Due to the fast energy consumption rate, the fossil fuels are currently decreasing, and nowadays human faces the challenges to use fossil fuels as major energy source.[1,2] Moreover, the harmful events resulted from fossil fuels, such as global warming, enforces people to find alternative, clean energy source.[1]

Nuclear energy is one of the alternative energy sources.[3,4] Currently, nuclear fission method has been applied for producing electrical energy using uranium source. The nuclear energy could theoretically provide 10 TW of energy which can take part 77 % of overall energy consumption in the world. [1, 3,4] However, when the nuclear energy will offers 10 TW of energy, terrestrial uranium source will be depleted within 10 years.[1,3,4] More seriously, the possible disaster resulted from the nuclear energy cannot be compensated as shown in the Chernobyl and Fukushima accident.

Wind power and bio-fuels has been developed for more safe future energy supplies than nuclear energy.[5,6] Wind power utilizes natural wind to generate energy using wind turbines and wind pumps. It requires relatively small efforts for construction because of its simple technology. Moreover, wind, the major source in this system, do not need cost and cannot be exhausted in the future.[1] Wind power market is currently increasing and generating about 2 % of total electricity in the world, nowadays.[1] Bio-fuels are methods to generate energy using living-organisms. Certain forms of bio-fuels are comparable to the energy from fossil fuels. (2-4 $cents/ KWh)[6]

Among the various alternative energy sources, solar energy is the most abundant and inexhaustible source.[7-15] 120,000 TW of radiation reaches at the earth which is 12,000 times higher than total energy consumption in the world.[1,7,8] There are various ways to utilize solar energy including solar thermal conversion, solar electricity, and solar fuels.[1] Among them, produce hydrogen and water molecules from water using solar energy has been regarded as the most advantageous method.[7-15] This method has tremendous advantages because it uses only water and solar energy as major component which is earth-abundant and non-exhaustive to generate hydrogen fuel. [7-15] Moreover, hydrogen molecules are the simplest energy carriers that exhibit the high energy density by weight which is around four times higher than fossil fuels[7-15]. In this regard, it has high potential for alternating conventional energy supply systems.

1.2 Water splitting

Splitting water to generate hydrogen and oxygen molecules is an environmentally friendly solar-to-energy conversion method.[7-15] The ultimate goal for water splitting is that store solar energy into simplest chemical fuel, hydrogen gas. [7-15]

The concept of water splitting was firstly inspired from the biological photosystem in plants. In photosystem, there are two subunits so called photosystem II and photosystem I. In photosystem II, the water is oxidized into oxygen catalyzed by Mn_4CaO_5 cluster.[16-21] The electrons arised from the water oxidation are then excited using visible light at two reaction centers (P_{700}, P_{680}). [16-21] Photo-excited electrons move to photosystem I through electron transport chain. [16-21] These electrons and surrounding hydrogen ions are incorporated with the $NADP^+$ (Nicotinamide adenine dinucleotide phosphate), and consequently reduced form of $NADP^+$, NADPH, is formed. [16-21] The reducing power NADPH was used for making glyceraldehyde 3-phosphate which is used as immediate nutrient in plant.[21]

Similar with the photosystem, water splitting basically can be categorized into two redox reactions. At the anode, water is oxidized into oxygen molecules, and hydrogen ions converted into hydrogen molecules using the electrons from the anode at the cathode.[22-23] This reaction can be summarized into following equations:

$2H_2O \rightarrow O_2 + 4H^+ + 4e^-$	E_{anodic} = - (1.23 – 0.0592 x pH) V vs. NHE
$4H^+ + 4e^- \rightarrow 2H_2$	$E_{cathodic}$ = (0 - 0.0592 x pH) V vs. NHE
$2H_2O \rightarrow 2H_2 + O_2$	E_{rxn} = - 1.23 V

Inspired by the photosystem, intensive researches have focused on developing photocatalysts for water splitting.[11-14,24] When the catalysts absorb the visible light, electrons and holes are generated at the conduction band and valence band of the catalysts, respectively.[11-14] The electrons at the conduction band and the holes at the valence band are used for hydrogen and oxygen production respectively.[11-14] Using the photocatalysts, without any applied voltage, water can be converted into hydrogen and oxygen molecules with only visible lights. [11-14] In 1970s, Fujishima group used TiO_2 as photocatalysts for water splitting for the first time.[24] After their work, a lot of photocatalysts for cathodic and anodic reaction have been developed.[11-14]

However, even after using photocatalysts, the catalytic performance of the catalysts was inferior because of the kinetic barrier.[22,25] This barrier is resulted from the nature of water splitting reaction that requires multi-electron and multi-step reactions.[22,23] Therefore, the electrocatalysts for both anodic and cathodic reaction must be designed to lower the activation energy and promote the efficiency of water splitting reaction. In this respect, there have been tremendous efforts to develop the electrocatalysts for water splitting and incorporate them with the photocatalysts.[22-66]

1.3 Oxygen Evolution reaction(OER)

The oxygen evolution reaction (OER) has been regarded as a rate-limiting step in realizing a fully integrated water-splitting system because of the high energy barrier for O-O bond formation.[22-23] Generally, mechanism for the OER at the surface of the metal oxides has been known as the following four electron involved reaction paths [25]:

(1) H_2O (l) + * → HO* + H^+ + e^-

(2) HO* → O* + H^+ + e^-

(3) O* + H_2O (l) → HOO* + H^+ + e^-

(4) HOO* → * + O_2 (g) + H^+ + e^-

where * is the active sites for OER catalysis. This catalytic mechanism has been revealed from Tafel analysis.[7,25] For example, the discharge of water molecules or hydroxyl ions to oxidize the active sites onto the surface of the catalysts results in Tafel slope value of 120 mV/dec.[7] Further chemical conversion into stable chemical species onto the active sites yields Tafel slope value of 60 mV/dec.[7]

In order to fundamentally understand the change in activity of OER electrocatalysts, many researches have proposed several theories.[26-29] In 1984, Rasiyah proposed that when redox potential of the catalyst is close to the

thermodynamic potential for OER, the catalysts should have high activity.[26] Trasatti proposed that the strength of metal-oxygen bonds onto the surface can be a good descriptor for predicting the catalytic activity.[27] And Otagawa group suggested that 3d electron number of the transition metal at the bulk structures can be related to the catalytic activity.[28]

Recently, Shao-horn Yang group found that e_g occupancy in surface transition metals can be another good descriptor.[29] They take some assumptions that e_g orbital at the surface of the catalyst can make the σ-bonding with the anion adsorbates onto the surface.[29] Therefore, the occupancy of e_g orbital can affect on the binding of oxygen-containing intermediate species during the OER. [29] Comparing the various perovskites materials which contains different e_g occupancy, they experimentally found that catalysts that have e_g value of 1.2 shows the highest catalytic activity. [29]

As another route, Norskov and Rossmeisl group theoretically understand the activity of the OER electrocatalysts using DFT calculations.[25] They found the free energy of the rate liming step in the overall OER reaction and the overpotential value for the OER. These two values can be written by following equations [25]:

$G_{OER} = \max [\ \Delta G_1^\circ, \Delta G_2^\circ, \Delta G_3^\circ, \Delta G_4^\circ]$

$\eta(\text{overpotential}) = (G_{OER}/e) - 1.23$

Interestingly, they found that difference between the binding energy of HOO* and OH* is nearly constant onto the various types of metal oxides surfaces. [25] This difference between two energies can be defined as the theoretically lowest overpotential for OER catalysis. [25] However, only a few catalysts can operate with this lowest overpotential. [25] Instead, they suggested that the difference between the binding energies of O* and OH* could be a origin for the overpotential for the most of the OER electrocatalysts. [25] Moreover, they found that this assumption could be applied to the experimental results studied in the previous reports well. [25]

1.3.1 Noble metal based OER electrocatalysts

For decades, noble metals (Ir, Ru) based materials have been utilized as OER electrocatalysts due to their excellent catalytic activity under basic condition.[30-34] For example, IrO_x exhibits 1 mA/cm^2 of OER current with the only 200mV of overpotential (1.43 V vs RHE) and small Tafel slope value of 40 mV/dec. RuO_2 anodes reaches 1 mA/cm^2 at the applied potential value of 1.36 V vs RHE and has also small Tafel slope of 40 mV/dec.[30] Trasatti group demonstrated that optimized metal-oxygen bond strength in RuO_2 and IrO_x resulted in their high OER catalytic activity.[27] Moreover, Norskov and Rossmeisl group theoretically explained the high activity of RuO_2 based on the difference between the binding energies of O* and OH* which is assumed as rate-limiting step in the overall water oxidation process.[25] Using DFT calculation, RuO_2 exhibits the minimum difference among the various transition metal based OER catalyst, confirming their theoretical origin of high activity.[25]

Another advantage of noble metal based OER catalysts is their stability during the OER.[31-35] They maintain their catalytic current over weeks without the degradation while some transition metal based anodes undergo severe phase transformation or corrosion during the OER.[31-35] Likewise, because of their long-term stability and high catalytic activity, noble metal based OER electrocatalysts have been recognized as promising anode

materials for overall water oxidation systems. [31-35]

However, their high cost remains major drawbacks in a practical usage. For specific, the prices of Ir and Ru are 200 $/oz and 57 $/oz, respectively, where those of Co, Mn, Ni, and Fe which are also used as OER electrocatalysts (see section 3.2.) are 0.79 $/oz 0.064 $/oz 0.53 $/oz and 0.0039 $/oz, respectively. Currently, the electrolysis of water demands around 3 $ for 1 kg of hydrogen while gas reforming requires around 0.3 ~ 1 $ for equal amount of hydrogen according to US Department of Energy. Therefore, to construct the new systems that can produce hydrogen with low cost, high-cost materials such as noble metal based OER electrocatalysts should be avoided.

1.3.2 Transition metal (Co,Ni,Cu,Fe) based OER Electrocatalysts

Precious metal oxides, such as RuO_2 and IrO_2, exhibit superb OER catalytic activity; however, their high price remains an unavoidable weakness. Therefore, the development of efficient, durable, and inexpensive alternative catalysts is desirable.

In this regard, intensive researches have focused on developing transition metal based OER electrocatalysts.[35-43] Nocera groups employed amorphous inorganic films containing Co atoms and phosphate anions.[22] The films were prepared by electrodeposition of Co - Pi films onto ITO substrate using phosphate buffer with Co(II) ions. Interestingly, the Co - Pi catalyst is formed *in situ* and operates water oxidation with moderate overpotential value (~430 mV) in neutral water under ambient conditions.[22] Moreover, the Co-Pi films have self-reparing characteristics that the films are continuously depositioned on the ITO substrate during the OER.[35]

Similar with Co-Pi films, they also presented Ni based amorphous films by electrodeposition method.[36] Instead of Co(II) ions and phosphate buffer, they used Ni(II) ions and borate buffer to make the films. Interestingly, the Ni-Bi catalyst is also formed *in situ* and catalyze the water oxidation reaction under the overpotential value of ~620 mV at pH 9.2.[36]

Inspired from the high catalytic activities of Co, Ni based amorphous films, Berlinguette group recently developed amorphous $Fe_{100-y-z}Co_yNi_zO_x$

films.[30] They utilized photochemical metal-organic deposition method to make the amorphous films under low-temperature. [30] This method can produce amorphous metal oxide films where metals are distributed homogeneously in the films. [30] Surprisingly, the catalytic ability of $Fe_{100-y-z}Co_yNi_zO_x$ films is similar to that of IrO_x catalysts under basic condition.[30]

Moreover, Other than amorphous metal oxide films, Hongjie Dai group synthesized the ultrathin, layered Ni-Fe based double hydroxide plates onto mildly oxidized CNT.[37] In this case, the Ni-Fe plates and CNT were utilized as the OER catalysts and working electrodes, respectively. [37] This system is found to be highly catalytic active which is comparable to conventionally used Ir based electrocatalysts under basic conditions. [37]

In order to systemically understand and compare the catalytic abilities of transition metal oxide electrocatalysts, Jaramillo groups synthesized various Co, Fe, Ni based electrocatalysts, including CoO_x, CoPi, $CoFeO_x$, NiO_x, $NiCeO_x$, $NiCoO_x$, $NiCuO_x$, $NiFeO_x$, and $NiLaO_x$.[38] The overpotential values of the catalysts where current density of the catalysts reached at the 10 mA/cm^2 were measured for comparison. [38] Under alkaline condition, it was observed that these catalysts can operate OER catalysis under moderate overpotential value between 350 mV and 430 mV. [38]

As another route, many researches has been developed the transition metal complexes which are comprised of transition metal and surrounding organic ligands.[39-40] The organic ligands were used to systemically arrange the transition metals and stabilize the local structure and the valency state of the

metals. [39-40] Due to the high controllability of the organic ligands, a lot of transition metal complexes, including mononuclear, binuclear, and multinuclear complexes, were developed and their catalytic abilities were evaluated.[39] Additionally, the complexes have been used as platforms for understanding the role of local structure of transition metal and surrounding ligands on OER catalysis. [39]

However, most of the complexes have difficulty in mass-production compared to transition metal based oxide films because the synthesis of organic ligands and complexes is not facile. [39] In this respect, ease of synthesis of surrounding organic ligands can be another breakthrough for commercializing the transition metal complexes for OER catalysis.

Recently, Meyer groups have demonstrated the possibility of polypeptides as ligating ligands for transition metals.[40] Triglycylglycine (TGG^{4-}) peptides and Cu(II) ions were self-assembled into [(TGG^{4-})Cu(II)-OH_2]$^{2-}$ catalysts. [40] The Cu-polypeptide complexes show high catalytic activity (TOF number of 33 s^{-1}) and stability (~5 hr) toward OER catalysis. [40] This new approach using polypeptide as surrounding ligands can pave the way for developing other transition metal based complexes more facile. [40]

Additionally, in order to improve the efficiency Photo Electrochemical (PEC) cell, amorphous transition metal oxides were incorporated with the photocatalysts.[41-43] Gratzel group employed photo-assisted electrodeposition method in order to deposit Co-Pi OER catalyst onto α-Fe_2O_3. [41] Using this photo-assisted electrodeposition approaches, Co-Pi

films can be uniformly deposited onto α-Fe_2O_3.[41] Due to their uniformity, Co-Pi / α-Fe_2O_3 PEC cell exhibits OER current of ~ 3 mA/cm^2 at 1.23 V *vs.* RHE under AM 1.5 G.[41]

Gamelin group also incorporated Co-Pi films onto the well known photoanode, W doped $BiVO_4$.[42] After Co-Pi films were deposited onto the photoanode, the onset potential of W doped $BiVO_4$ was largely shifted (~ 440 mV) toward the cathodic direction, indicating highly enhanced catalytic activity.[42] The enhanced catalytic ability of this system mainly results from that the Co-Pi films which suppress the electron-hole recombination in $BiVO_4$ effectively.[42]

Recently, Wang group also performed similar studies using amorphous $NiFeO_x$ films which is developed by Berlinguette group.[43] They deposited the amorphous films onto hematite, and found that the a-$NiFeO_x$/hematite system can present very low onset potential of 0.62 V vs RHE.[43]

Likewise, the transition metal based OER catalysts have been incorporated with the photoanodes, and they dramatically have been enhancing the activity of photoanodes to realize the overall water splitting photoelectrochemical (PEC) cells.[41-43]

1.4 Manganese based OER electrocatalysts

1.4.1 Photosystem II in biological system

In nature, there is a water oxidation complex (WOC) in photosystem II (PSII) comprised of the earth-abundant elements Mn and Ca.[16-21] The WOC in PSII, in the form of a cubical $CaMn_4O_5$ cluster, efficiently catalyzes water oxidation under neutral conditions with extremely low overpotential value (~160 mV) and a high TOF number (~25,000 $mmol_{O2}\, mol^{-1}_{Mn}\, s^{-1}$). [16-21] The low overpotential value and high TOF number of WOC cannot be achieved with the any artificially developed electrocatalyts. [16-21]

Recently, X-ray analysis of the PSII structure at a resolution of 1.9 Å provided detailed structural information about a cubical Mn_4CaO_5 cluster stabilized by a surrounding peptide ligand.[19] Four Mn atoms are oxo-bridged in asymmetric positions and undergo successive changes in oxidation state, taking part in a so-called Kok cycle. [19,21] It was also suggested that O-O bond formation occurs at specific sites in the Mn_4CaO_5 cluster.[19]

1.4.2 Bio-inspired Mn based OER electrocatalysts

The unique capabilities of the cubical Mn_4CaO_5 cluster have inspired the design of many synthetic catalysts for the OER.[44-49] Especially researches have been focused on the asymmetric geometry and mixed valent (III/IV) states of Mn atoms in the WOC. [44-49] For example, the geometry of oxo-bridged Mn atoms has been synthetically controlled by designed organic ligands. $[Mn_4O_4L_6]^+$(L =$(MeOPh)_2PO_2$) or $[Mn_4O_4L_6]^+$- Nafion system have been recently demonstrated as efficient water oxidation catalysts.[44-45]

Agapie group has been synthesized $[Mn_3CaO_4]^{6+}$ core structure which is almost identical to that of the WOC in nature by using a trinucleating ligand.[46] This was the first work that mimics the local Mn geometry of the WOC nearly perfect. [46] Moreover, using the $[Mn_3CaO_4]^{6+}$ core structure, they further synthesized $Mn_3M(\mu_4\text{-}O)(\mu_2\text{-}O)$ (M = Ca^{2+}, Sr^{2+}, Na^+, Zn^{2+}, Y^{3+}) to understand the role of redox-inactive metals on water oxidation catalysis.[47] By comparing their catalysts, they found than redox inactive metals (M) can modulate the redox potential of Mn atoms. [47] From this result, they make an conclusion that Ca ions might change the redox potential of Mn atoms in the WOC, and consequently enhances the catalytic ability of the WOC. [47] (Figure 1.4.1)

As another route, inspired by the WOC, various crystalline manganese oxide polymorphs and amorphous MnO_x have been developed as

water oxidation catalysts.[48-53] Demonstration of calcium manganese compounds, such as $CaMn_2O_4$-$4H_2O$, as an improved water oxidation catalyst also represents a bio-inspired effort to mimic the natural Mn_4CaO_5 cluster.[48]

Dismukes group mimicked the $[Mn_4O_4]$ core units in the WOC by removing Li ions from $LiMn_2O_4$ Li-ion battery cathode material.[54] Catalytic inactive $LiMn_2O_4$ materials converted into the active λ-MnO_2 which has $[Mn_4O_4]$ core unit.[54] They assumed that $[Mn_4O_4]$ core unit in theλ-MnO_2 is the origin of its high catalytic activity.[54] (Figure 1.4.2)

Recently, Driess group developed amorphous MnO_x nanoparticles whose local structure and valence state of Mn atoms resemble with those of the WOC.[55] They oxidized inactive, crystalline MnO nanoparticles into active, amorphous MnO_x ($1 < x < 2$) using Ce^{IV} oxidants.[55]

Interestingly, according to some reports, although they did not intend to mimic the Mn_4CaO_5 cluster, they found that high activity of their catalysts is originated from the Mn structure and valence state which was very similar with those of the Mn_4CaO_5 cluster.[53,56] For example, Dau group developed new electrodeposition method which can present active MnO_x film.[53] This new film shows much higher activity than conventionally electrodeposited films. Using EXAFS and XANES analysis, they found that the newly developed electrodeposited amorphous MnO_x films have mixed valent state (III/IV) and disordered Mn geometry which are recognized as important properties of the WOC in nature.[53] Similarly, Jaramillo group found that the

active manganese oxide catalysts have mixed valency state of Mn(III/IV) that is similar with the valency state in the Mn_4CaO_5 in photosystem II.[56]

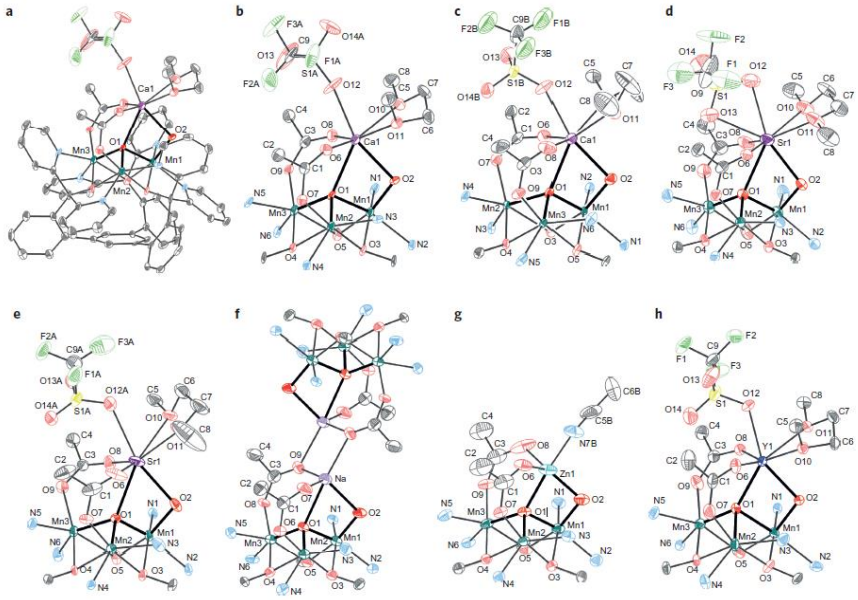

Figure 1.4 1 Solid-state structures of bio-inspired reported $Mn_3M(\mu_4\text{-}O)(\mu_2\text{-}O)$ (M = Ca^{2+}, Sr^{2+}, Na^{+}, Zn^{2+}, Y^{3+}) complexes developed by Agapie groups. Figure was reproduced from [47]

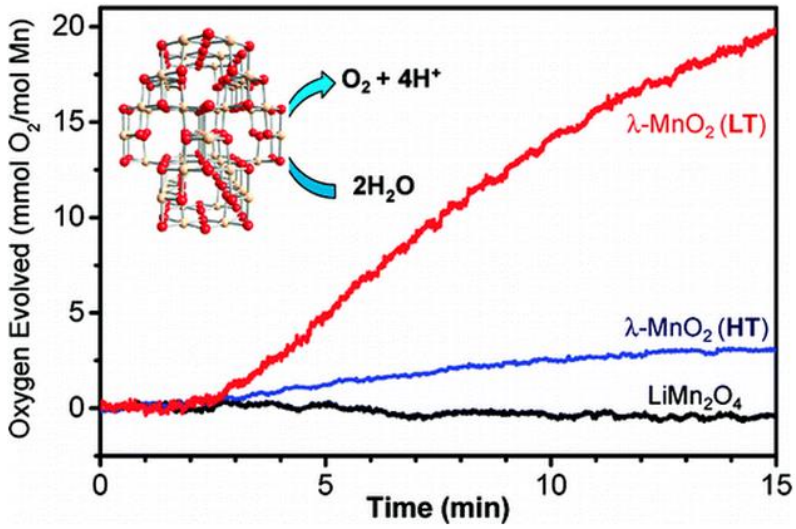

Figure 1.4 2 High catalytic activity of λ-MnO_2 compared to $LiMn_2O_4$. λ-MnO_2 can be obtained by delithiation from $LiMn_2O_4$. Inset shows the crystal structure of λ-MnO_2. The [Mn_4O_4] core units resembles with the structure of the Mn_4CaO_5 clsuter in photosystem II. This work was done by Dismukes group. Figure was reproduced from [54]

1.4.3 Bottleneck in Mn based electrocatalysts in OER

Unlike the WOC in nature, the catalytic properties of Mn oxide compounds degrade drastically at neutral pH. The electro-catalytic performance of most Mn-based catalysts is degraded significantly at neutral pH.[57-60] For example, the overpotential values of Mn_2O_3 and MnO_2 at pH 7 range from 500 to 700 mV, whereas it is approximately 300 mV at pH 14. [57-60]

Previous works on manganese-containing catalysts have experimentally and theoretically emphasized the role of Mn(III) as an important intermediate state to enable the catalytic reaction. [57-60] Irrespective of the initial manganese oxidation states in catalysts, Mn(III) is generated and participates in water oxidation process.[57-60] However, considering the electronic configuration, Mn(III) (t_{2g}^3 e_g^1) accompanies strong Jahn-Teller distortion and tends to break the symmetry of the orbitals; thus, this state is not stable in symmetric octahedral structures.[57-61] In this respect, many previous studies have suggested that the degradation of manganese-based catalysts results from Mn(III) disproportionation into Mn(II) and Mn(IV) in neutral water losing its catalytic property.[57,60]

1.4.4 Importance for understanding the effect of Mn Valency And Structure on water oxidation catalysis

Rigid and highly symmetric MnO_6 octahedrons in MnO_2 compounds hamper Jahn-Teller (J-T) distortion in the local coordination environment of Mn centers. [57,60] Thus, Mn(II) and Mn(IV) cannot be easily oxidized or reduced to Mn(III), which is an important intermediate during oxygen evolution. [57,60] Inversely, Mn(III)-containing Mn oxide compounds, such as Mn_2O_3, cannot easily change valence state due to the high reorganizational energy associated with Mn(III) oxidation.[63-64] Similar phenomena can be found in the Ni(III)-Bi catalysts.[65] Non-anodized Ni(III)-Bi catalysts have properties inferior (Tafel slope: 100 mV/dec) to those of their anodized counterparts because of the reorganization energy required to oxidize J-T distorted Ni(III) to non-distorted Ni (IV).[65] Therefore, the fundamental challenge is how to flexibly change the valence state of Mn atoms with ease and stabilize Mn(III) state in a crystal structure during oxygen evolution at neutral pH.

A phosphate group could help to provide a solution for the problems outlined above. Transition metal-phosphate compounds have been investigated as cathode materials for Li-ion batteries for decades.[66-68] Typically, these materials display more distorted structures than metal oxides because the phosphate group has a bulky tetrahedral geometry, which tends to

break the crystallographic symmetry. [66-68] (Table S1 in the Supporting Information). Additionally, there are few reports that use only divalent manganese as the resting state for electro-catalysis because of the widely held assumption that high valency in inorganic compounds should be beneficial for catalytic performance. In the Chapter 2, in an effort to achieve an asymmetric arrangement of manganese atoms with flexible Mn–O bonding, we have synthesized a new divalent manganese phosphate hydrate and investigated the detailed process of how the valence changes during water oxidation. Moreover, we explore the possibility of using divalent manganese with a phosphate anion as a resting state for water oxidation.

Moreover, based on such a theoretical approach, there have been many pioneering studies to stabilize Mn(III) and to understand the role of manganese ions to enhance catalytic activity. For example, the Nakamura group stabilized the Mn(III) state by introducing partial asymmetry to the crystal field in MnO_2 through nitrogen doping, and promoted the water catalysis of MnO_2.[60] The Dau group synthesized amorphous Mn-oxide films with distorted, corner-sharing MnO_6 octahedra to stabilize Mn(III) sites.[53] Moreover, the effect of manganese crystal environments on the catalytic role was recently investigated by the Dismukes group.[70] They comparatively studied eight different manganese oxides, including Mn_2O_3, Mn_3O_4, β-MnO_2, λ-MnO_2, and $LiMn_2O_4$, and found that the catalytic activity generally enhances when Mn-O bonds are weak/distorted and Mn-Mn distances are

long in the structure.[70] It was also shown that $LiMn_2O_4$ composed of Mn(III) and Mn(IV) atoms has no catalytic activity, while λ-MnO_2, which does not contain Mn(III) atoms, exhibits high catalytic activity.[70] All of these works suggest that not only Mn valency but also structural factors, such as the crystal framework and the Mn geometry, are mutually important in determining the catalytic activity.[53,60,70]

However, in understanding the catalytic activities of these manganese-based compounds, it seems not trivial to decouple the effect of the Mn valency and structural factors. Typically, the crystal systems of Mn(III)-containing oxides are different from those of Mn(IV)- or Mn(II)-based oxides.[61] Thus, comparing these two systems with different manganese oxidation states inevitably involves the influence of the manganese local environments in each crystal systems.[61] A question that we attempt to understand in this study is whether the catalytic property will change with the variation of Mn valency when maintaining the same structural factors. We decoupled the two factors and obtained a clue to understanding how Mn valency affects water catalysis. In Chapter 3, we have selected $Li_2MnP_2O_7$ as a model system. The notable capability of $Li_2MnP_2O_7$ is that the oxidation state of Mn can be accurately adjusted from two to three by controlled delithiation with minimum structural change.[71] Other manganese oxide/phosphate-based lithium intercalation materials typically undergo significant phase separation or transformation during delithiation.[72-73] For example, $LiMnPO_4$ phase

separates into $LiMnPO_4$ and $MnPO_4$ upon delithiation.[72] $LiMn_2O_4$ also transforms by two-phase reaction into $Li_{0.5}Mn_2O_4$ or λ-MnO_2 during delithiation.[73] Another reason why we chose $Li_2MnP_2O_7$ as a catalyst is that the pyrophosphate group itself has unique advantages in distorting Mn geometry due to its asymmetric nature.[74-79] While it is hard to achieve with conventional Mn oxide compounds, a distorted local crystal structure in $Li_2MnP_2O_7$ is expected to be favorable for the catalytic cycle. Moreover, the pyrophosphate group has been used as a stabilizing agent for the Mn(III) state via specific chelating reactions under neutral pH.[60]

Chapter 2. $Mn_3(PO_4)_2$-$3H_2O$

: Effect on Mn structure on OER catalysis

2.1 Experimental and Procedure

2.1.1 Synthesis and Materials

$MnCl_2$-**4**H_2O (99 %), HEPES (2-4-(2-hydroxyethyl)-1-piperazinyl)Ethane-sulfonic acid) (99 %), KH_2PO_4 (99 %), $Na_4P_2O_7$ (95 %), PVDF(Polyvinylidene difluoride, average M_w ~530,000, pellets), Nafion 117 solution (5 wt % in aliphatic alcohols and water), NMP(1-Methyl-2-pyrrolidinone, 99.5 %) solution, $Na_2S_2O_8$ powder (>98 %), $Ru(bpy)_3$-**6**H_2O (Tris(2,2'-bipyridyl) dichloro-ruthenium(II) hexahydrate) (99.95 % trace metal basis), MnO_2 (99.99 %), MnO (99.99%), Na_2HPO_4-**7**H_2O (ACS reagent, 98.0-102.0 %), Isopropyl alcohol (99.7 %), NaOH (98.0 %), and NaH_2PO_4-**2**H_2O (99.0 %) were purchased from Sigma Aldrich and used as received without further purification. Fluorine doped Tin-Oxide coated glass (FTO, TEC-8) which has 15 Ω sq^{-1} surface resistivity was obtained as pre-cut by 1.0 cm × 1.5 cm glass pieces from Pilington Company.

Manganese (II) phosphate hydrate was synthesized by adding 40 ml

of 1.0 mM KH_2PO_4 in HEPES (1.85 mM, pH 7.4) to 40 mL of 1.0 mM $MnCl_2$-**4**H_2O solution at 37℃. The mixed solution slowly became turbid, indicating the formation of manganese (II) phosphate hydrate. After 3 h, the precipitate was centrifuged and washed three times with deionized (DI) water. Collected particles were then lyophilized before characterization.

2.1.2 Characterization

2.1.2.1 Powder X-ray diffraction

Powder X-ray diffraction (XRD) was carried out on a D-8 Advance X-ray diffractometer with Cu Kα radiation (λ=1.54056Å). For the measurement, precipitated $Mn_3(PO_4)_2$-**3**H_2O powder was collected and lyophilized at least 2 days. The lyophilized powder was loaded on Si holder, retrofitted in X-ray diffractometer. XRD patterns were recorded in a range of 5 ~ 100° with a step of 0.02° and a velocity of 0.02°/16 s. Obtained XRD patterns were compared with previously reported JDPDS cards.

2.1.2.2 ICP/MS

Inductively Coupled Plasma-Mass Spectrometer (ICP/MS, 720-ES, Varian) measurement was conducted to determine the exact chemical

composition of $Mn_3(PO_4)_2$-**3**H_2O.

Thermo Gravimetric analysis (TGA) was performed on the lyophilized $Mn_3(PO_4)_2$-$3H_2O$ powder described above. 2.177 mg of the samples were loaded to Thermo gravimetric analyzer(Q-5000 IR, TA instrument, USA) and its weight loss measured in a range of 25~500℃ with 5℃ min^{-1}

2.1.2.3 Rietveld analysis

The crystal structure of switzerite was obtained from American Mineralogist Crystal Structure Database (AMCSD). The presumed crystal structure of the $Mn_3(PO_4)_2$-**3**H_2O was drawn with CrystalMaker (CrystalMaker Software) based on its atom coordination information. The maximum bond length between manganese atom and oxygen atom was set to 2.5 Å. Local structure around the P(1) site was visualized by defining the spherical cluster around the P(1) site at the radius of 4.5 Å. The final structure of $Mn_3(PO_4)_2$-**3**H_2O was refined by Rietveld refinement using TOPAS Academic.

2.1.2.4 Scanning electron microscopy(SEM) analysis

The morphology of synthesized $Mn_3(PO_4)_2$-**3**H_2O was characterized

with a high resolution scanning electron microscope (Supra 55VP, Carl Zeiss, Germany). The samples were investigated right after the electrochemical measurements or formation of $Mn_3(PO_4)_2$-**3**H_2O flower like plates on FTO glasses. The samples were rinsed gently with deionized water at least 3 times and dried with nitrogen gas. Pt coating was done by Pt Sputter Coater (BAL-TEC/SCD 005) because $Mn_3(PO_4)_2$-**3**H_2O particles were not conductive enough. Images were taken with an acceleration voltage of 2 kV, and EDX spectra with a 15 kV. Sample positions coincided with the illuminated area.

2.1.2.5 Transmission electron microscopy(TEM) analysis

TEM images and selected area electron diffraction (SAED) patterns were obtained using a high resolution transmission electron microscope (JEM-3000F, JEOL, Japan) with an acceleration voltage of 300 kV. The TEM samples were collected from FTO glass right after the catalyst formation or electrochemical measurement, and dispersed in ethanol by sonication about 1 min. About 10 μl of dispersed $Mn_3(PO_4)_2$-**3**H_2O were dropped on the TEM grid and dried in an oven.

2.1.2.6 Brunauer–Emmett–Teller (BET) method

Brunauer-Emmett-Teller (BET) analysis was conducted on the

lyophilized $Mn_3(PO_4)_2$-**3**H_2O powder. 0.5070 g of the sample was loaded to BET analyzer (Physisorption Analyzer, micromeritics, USA) under N_2 adsorption environment.

2.1.3 Electrochemical analysis

2.1.3.1 Cyclic Voltammetry (CV)

All electrochemical experiments were conducted under a three-electrode electrochemical cell system. A BASi Ag/AgCl/3M NaCl reference electrode and a Pt foil (2 cm × 2 cm × 0.1 mm, 99.997% purity, Alfa Aesar) were used as a reference electrode and a counter electrode, respectively. Electrochemical tests were carried out at ambient temperature using a potentiostat system (CHI 600D, CH Instruments). Electrode potential was converted to the NHE scale, using the following equation: E(NHE) = E(Ag/AgCl) + 0.197 V. Additionally, overpotential values were calculated by the difference between the iR corrected potential ($V = V_{applied} - iR$) and the thermodynamic point of water oxidation at a specified pH. The electrolyte was phosphate buffer with 500mM buffer strength under the pH 7. The electrolyte was degassed by bubbling with high-purity nitrogen (99.999 %) for at least 1 hour prior to the start of each experiment and stirred vigirously during the measurement to prevent the mass trasfort problem..

The preparation procedure of the working electrodes containing our catalysts can be found as follows. Firstly, 5 mg of catalyst powder was dispersed in 1 ml of water mixed solvent with 100 μl of neutralized Nafion solution. Then the mixture was sonicated for at least 30 min to make homogeneous ink. Next, 50 μl of the catalyst solution was dropped onto the

FTO substrate and spin-coating was performed at 3000 rpm for 30sec. Finally, prepared working electrode was dried at 80℃ oven before CV measurement. The working electrode was cycled at least 3 times with the potential stepped from 0.7 V to 1.5 V without pause at a scan rate of 10 mV sec^{-1} before all electrochemical data were recorded. Prior to every electrochemical experiment, the solution resistance was measured in the electrolysis bath. All the data were iR-compensated.

2.1.3.2 Gas Chromatography (GC)

The photo-oxidation reactions for O_2 evolution were conducted in an outer-irradiation-type quartz reactor (120 ml) with a closed circulating gas system at ambient temperature. The UV light source was a 450 W high-pressure mercury lamp maintaining a distance of 15 cm between the reactor and the lamp. The lamp was surrounded by a circulating cooling water jacket. In the quartz reactor, 6 mg of $Mn_3(PO_4)_2$-$3H_2O$, solid $[Ru(bpy)_3]Cl_2$, and $Na_2S_2O_8$ (final concentrations 1.5 mM $[Ru(bpy)_3]Cl_2$ and 12.5 mM $Na_2S_2O_8$ in the sample solution) were dispersed together in a 25 ml phosphate buffer (100 mM, pH 7). The solution was stirred and sonicated at least 30 minutes respectively to allow complete dispersion. During the stirring and the sonication, the reactor was covered with aluminum foil to prevent irradiation

of light. After the reactor connected with the closed gas circulation system inside, the solution was purged with high-purity Ar gas (99.999 %) for 30 minutes before irradiation. The amount of evolved O_2 was recorded every 5 minutes via gas chromatography (DS6200, Donam, Korea). Additionally, the control experiment was also carried out, wherein no $[Ru(bpy)_3]Cl_2$ was contained in the reactor. The TOF number was calculated and compared with other manganese based catalysts.

2.1.4 Electron paramagnetic resonance (EPR) spectroscopy

All EPR measurements were carried out at KBSI, Daejeon, Korea. Electron paramagnetic resonance (EPR) was performed using a Bruker EMX/Plus spectrometer equipped with a dual mode cavity (ER 4116DM). Low temperatures were achieved and controlled using a liquid He quartz cryostat (Oxford Instruments ESR900) with an temperature and gas flow controller (Oxford Instruments ITC503). The experimental conditions are as follows. Microwave frequency 9.64 GHz (perpendicular mode), 9.4 GHz (parallel mode), modulation amplitude 10G, modulation frequency 100 kHz microwave power 0.94 mW (perpendicular mode), 5.0 mW (parallel mode) temperature 5.7K. 10 scans were added for each spectrum.

All the $Mn_3(PO_4)_2$-**3**H_2O samples were loaded on FTO glass (1.5 cm × 2.5 cm) in the form of carbon paste. In order to obtain carbon paste, we mixed $Mn_3(PO_4)_2$-**3**H_2O, PVDF, carbon in the ratio of 8:1:1(weight ratio), and then 100μl NMP solution was dropped on the mixture. The paste was loaded on the FTO substrate carefully by blade and dried in the 80℃ oven. To eliminate residual Mn^{III} ion on the surface of $Mn_3(PO_4)_2$-**3**H_2O, the paste-loaded FTO glass was dipped in 20 mM pyrophosphate solution at least 30 minutes and gently rinsed with deionized water prior to bulk electrolysis.

The bulk electrolysis was conducted using a cyclic voltammetry system (CHI 760D, CH Instruments, Inc.) under pH 7, 500 mM sodium

phosphate buffer solution. Designed potentials were applied to each sample for 30 minutes, respectively. After the bulk electrolysis, the samples were rinsed gently by deionized water and transferred to an EPR tube by blade under Ar (99.999 %) atmosphere as promptly as possible. The EPR tube was frozen and stored at 77K in liquid nitrogen immediately.

2.1.5 DFT calculation

The first-principles density functional theory (DFT) calculations were performed with GGA+U functional using the Vienna *Ab*-initio simulation package (VASP) code. Electron-ion interactions were approximated by the projected augmented wave (PAW) method. The effective *U* parameter of 4.0 eV was used for Mn d orbitals. The cutoff energy for plane-wave basis set was consistently chosen to be 800 eV, and the k-space was sampled by a 2 × 2 × 2 regular mesh. Atomic positions and lattice parameters were relaxed until the force and stress were reduced below 0.02 eV $Å^{-1}$ and 2 kbar. The atomic charges were estimated by the Bader analysis for prisine $Mn_3(PO_4)_2$-**3**H_2O, oxidized Mn phosphate, β-MnO_2, and reduced Mn oxide.

2.2 Results and Discussions

2.2.1 Structural Characterization of $Mn_3(PO_4)_2$-$3H_2O$

ICP-MS measurements and TGA revealed that the ratio of manganese atoms to phosphorous atoms in the manganese (II) phosphate hydrate crystal is 3:2 and that three water molecules are embedded per unit cell inside the crystal structure (Figure 2.1). X-ray diffraction (XRD) analysis confirmed that the crystal structure of synthesized manganese phosphate is $Mn_3(PO_4)_2$-$3H_2O$. In this study, we discovered a new crystal, $Mn_3(PO_4)_2$-$3H_2O$, whose crystal structure has never been identified completely. First, we tried to match our diffraction pattern with the available crystal structures in the Inorganic Crystal Structure Database (ICSD), but the existing JCPDS data did not provide a match. Among the available data, the most similar pattern comes from JCPDS card No. 00-003-0426 (quality mark: low precision (O)) for poorly crystalline $Mn_3(PO_4)_2$-$3H_2O$ (Figure 2.2 and Table 2.1). However, there is no crystallographic information available, such as the lattice parameter, atom coordination, Z-factor and plane index. Therefore, we determined the accurate crystal structure of $Mn_3(PO_4)_2$-$3H_2O$ by performing Rietveld refinement analysis and density-functional theory (DFT) calculations, and we compared simulated diffraction data with the experimental data (Figure 2.5d).

To computationally determine the crystal structure of $Mn_3(PO_4)_2$-$3H_2O$, we focused on the crystal structure of switzerite ($Mn_3(PO_4)_2$-$7H_2O$), which had been determined previously.[69] Since the position of H atoms or orientation of water molecules were not well resolved in experiment, we annealed the initial switzerite structure at 300 K during 3 ps using the first-principles molecular dynamics (MD) simulation subsequently relaxed the structure at 0 K, obtaining the theoretical lattice parameters and atomic positions at equilibrium. According to the previous study, switzerite can transform to metaswitzerite ($Mn_3(PO_4)_2$-xH_2O, $3 < x < 4$) by expelling some water molecules and condensing the neutral layers along *c* in the framework structure.[69] The transformation is topotactic; only a minor change in atomic position occurs during dehydration.[69] Thus, in our first attempt to determine the structure, we assumed that the crystal structure of $Mn_3(PO_4)_2$-$3H_2O$ can be derived in a topotactic manner by removing four water molecules from switzerite. From the TGA analysis, we knew that there should be three water molecules per $Mn_3(PO_4)_2$.

Starting from the switzerite structure, we first removed three water molecules per formula unit in various combinations consistent with the structural information provided in ref 69. These structures were then fully relaxed using density functional theory (DFT) methods and the lowest-energy structure was chosen as the metaswitzerite. We then removed one additional water molecule per formula unit in every possible way and relaxed the structure again. The most stable structure was regarded as the theoretical

structure of $Mn_3(PO_4)_2$-$3H_2O$, which is triclinic, P1, with a = 8.640(3) Å, b = 13.354(8) Å c = 8.455(1) Å α= 86.50(1)° β= 105.12(5)° γ= 90.14(3)° and Z = 4. All of the peaks obtained experimentally can be matched with those obtained from the simulated crystal structure

Close observation of the newly identified $Mn_3(PO_4)_2$-$3H_2O$ crystals allows us to distinguish six different manganese sites in one unit cell (Figure 2.3). As shown in Figure 2.3, the surrounding geometry of each manganese is symmetrically broken because $Mn_3(PO_4)_2$-$3H_2O$ has triclinic crystal systems with the lowest symmetry. For example, Mn(1), Mn(2), Mn(3) and Mn(4) have distorted octahedral coordination, whereas Mn(5) and Mn(6) have distorted trigonal bipyramidal (TBP) geometry (Figure 2.3).

Water molecules are also positioned differently inside one unit cell ($[Mn_3(PO_4)_2$-$3H_2O]_4$, Z = 4). Of the 12 water molecules in each unit cell, eight water molecules (water 1) participate in bridging two manganese atoms in a Mn(1, 2, 3 and 4) sheet. Two water molecules (water 2) are bound to Mn(6). The other two water molecules (water 3) stay between two sheets of Mn(1, 2, 3 and 4) without forming any coordinated bonds (Figure 2.4).

The asymmetric geometry of each manganese atom can be observed clearly by displaying the local structure around the P(1) position (Figure 2.1e). We measured the distances between manganese atoms in the simulated crystal structure. The shortest distance is 3.348 Å, between Mn(2) and Mn(3), and the longest one is 6.408 Å, between Mn (3) and Mn(5) in the local structure

around the P(1) position. The average Mn-Mn distance is 3.411 Å, and the average Mn-O distance is 2.215 Å, which is much longer than the distances reported previously for Mn oxide-based compounds.[70] (Table 2.2 and Table 2.3). In PSII, the Mn_4CaO_5 cluster also has an asymmetric geometry, distorted chair form and different distances between the four manganese atoms. In the cluster, the shortest distance is 2.8 Å, and the longest is 5.4 Å.[19]

$Mn_3(PO_4)_2$-$3H_2O$ crystals prefer to grow in sheet-like structures under our experimental conditions. When the fluorine-doped tin oxide (FTO) glass is dipped during the synthesis of $Mn_3(PO_4)_2$-$3H_2O$, the sheets that can be found in bulk solution are assembled into a flower-like morphology, as shown in Figure 2.5a,b. High-resolution transmission electron microscopy (HRTEM) and selective area electron diffraction (SAED) analysis reveal that the two axes in the rectangular sheet are aligned in the [001] and [010] directions (Figure 2.5c and Figure 2.5c inset).

Oxide compound	System	Phosphate compound	System
MnO	Cubic (Fm3m)	**$Mn_2P_2O_7$**	Monoclinic(C2/m)
Mn_2O_3	Orthorhombic (P bca)	**$Mn_3(PO_4)_2$**	Monoclinic($P2_1/a$)
MnOOH	Monoclinic ($B2_1/d$)	**MnP_4O_{11}**	Triclinic ($P\bar{1}$)
Mn_3O_4	Tetragonal ($I\ 4_1/amd$)	**$Mn_2P_4O_{12}$**	Monoclinic (C2/c)
MnO_2	Tetragonal ($P4_2/mnm$)	**$Mn_3(PO4)_2$**	Monoclinic ($C2_1/c$)
$MnFe_2O_4$	Tetragonal ($P4_2/nnm$)	**$Mn(PO_3)_3$**	Orthorhombic (Pnaa)
CoMnO	Cubic, Tetragonal ($I4_1/amd$)	**$Mn_3(PO_4)_2$ - $3H_2O$**	Triclinic (Our work)

Table 2. 1 Crystal structures of manganese based oxide and phosphate compounds. It showed that almost all manganese oxide compounds display higher symmetry than manganese phosphate compounds. (All data were referred from JCPDS Card.)

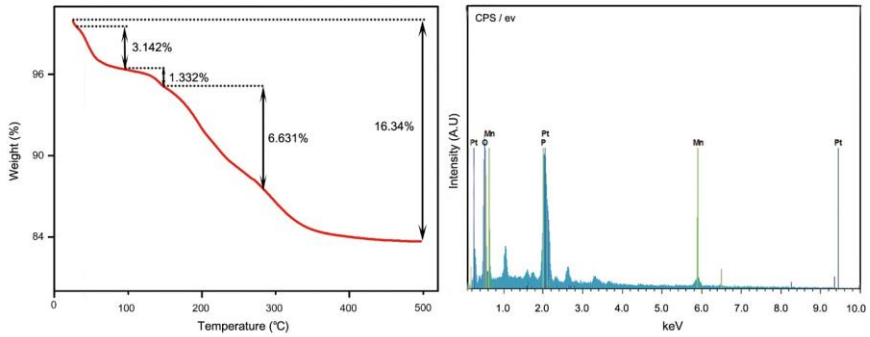

	Atomic weight	Solution concentration	Molar ratio
Mn	54.938	6.92	3
P	30.974	2.49	1,92

Figure 2. 1 Thermogravimetric analysis (TGA) of $Mn_3(PO_4)_2$-$3H_2O$ from 25℃ to 500℃. The first drop of weight showed evaporation of H_2O molecules attached on the surface. Sequential weight drops of $Mn_3(PO_4)_2$-$\mathbf{3}H_2O$ indicated that H_2O molecules were intercalated in $Mn_3(PO_4)_2$-$\mathbf{3}H_2O$ structure. With the total weight loss (13.198 %) during TGA analysis, except that generated by surface water molecules, we could draw that three H_2O were embedded in manganese phosphate structure. And we also obtained from the ICP-MS result and EDS analysis that the ratio of manganese and phosphate was 3:2. Based on these results, we concluded that chemical formula of our catalyst was $Mn_3(PO_4)_2$-$\mathbf{3}H_2O$.

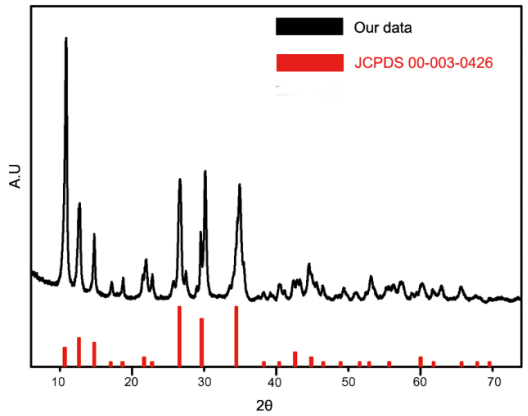

JCPDS 00-003-0426	Comments
Experimental Reference	The Dow Chemical Company, Midland, Michigan, USA. *Private Communication*
Chemical Formula	$Mn_3(PO_4)_2$-**3**H_2O
Empirical Formula	H6Mn3O11P2
Weight %	H1.48 Mn40.32 O43.05 P15.15
Atomic %	H27.27 Mn13.64 O50.00 P9.09
Physical Information	None
Crystal Information	None (Molecular weight = 408.8)
Structure Data	None (Centrosymmetric)

Figure 2. 2 Comparison between XRD pattern of our $Mn_3(PO_4)_2$-**3**H_2O and previously reported JCPDS pattern of $Mn_3(PO_4)_2$-**3**H_2O. The JCPDS card data was significantly different from our data in terms of peak positions and peak intensity.

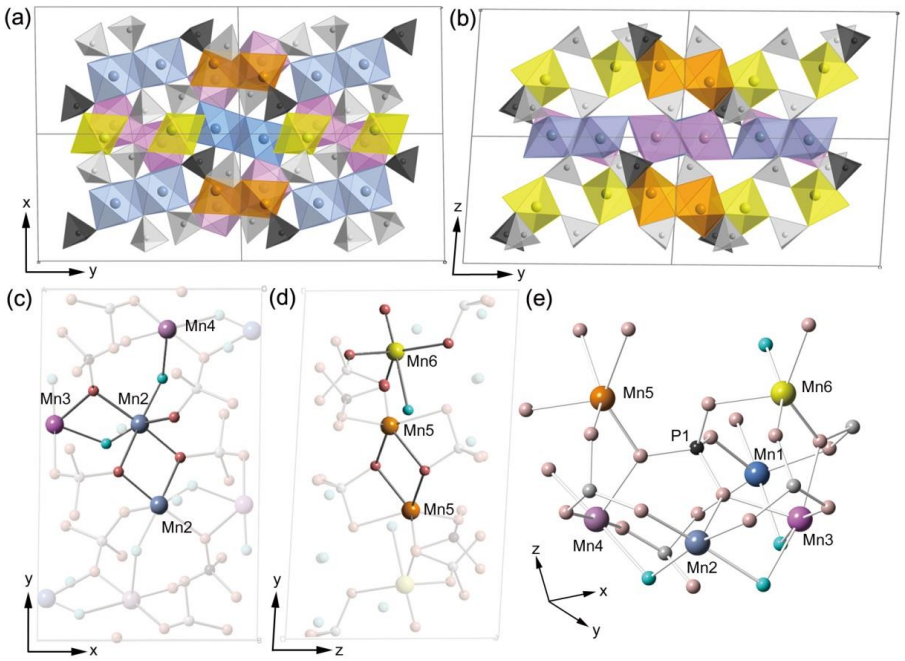

Figure 2. 3 Schematic representation of crystalline $Mn_3(PO_4)_2$-$3H_2O$. (a. b) Coordination and arrangement of each manganese atom. Larger spheres denote Mn atoms, and smaller spheres denote phosphate atoms. (c) Mn(2) atoms are connected to each other by edge O-O sharing. Mn(2) and Mn(3) atoms are bridged by edge O-O_w sharing, and Mn(2) atoms are linked to Mn(4) atoms by O_w vertex sharing. (O_w : Oxygen atom in a water molecule) (d) Bonding character of Mn(5) and Mn(6). The Mn(5) atoms share two oxygen atoms with each other whereas the Mn(6) atom does not share any atoms with other manganese atoms. (e) Spherical cluster around the P(1) site, with a radius of 4.5 Å illustrating the asymmetrical arrangement of the manganese atoms.

Mn1	Mn2	Mn3	Mn4	Mn5	Mn6
2.210 Å	2.286 Å	2.163 Å	2.259 Å	2.214 Å	2.177 Å
2.145 Å	2.173 Å	2.286 Å	2.281 Å	2.208 Å	2.104 Å
2.119 Å	2.359 Å	2.262 Å	2.147 Å	2.316 Å	2.108 Å
2.317 Å	2.240 Å	2.218 Å	2.171 Å	2.120 Å	2.135 Å
2.139 Å	2.117 Å	2.264 Å	2.215 Å	2.121 Å	2.442 Å
2.468 Å	2.164 Å	2.175 Å	2.180 Å		

Table 2. 2 Bond lengths between manganese and neighboring oxygen atoms in $Mn_3(PO_4)_2$-**3**H_2O. Average Mn-O bond distance is 2.215 Å

	Mn1	Mn2	Mn3	Mn4	Mn5
Edge	3.259 Å	3.348 Å	3.348 Å	3.398 Å	3.526 Å
Sharing	3.398 Å	3.208 Å	3.295 Å	3.337 Å	
Corner	3.664 Å	3.718 Å	3.664 Å	3.718 Å	3.609 Å
Sharing				3.609 Å	

Table 2. 3 Mn-Mn distance in $Mn_3(PO_4)_2$-**3**H_2O. Distance values between edge-sharing manganese atoms and corner-sharing manganese atoms were obtained. Average Mn-Mn bond distance was 3.412 Å. Generally, corner sharing manganese atoms had larger Mn-Mn distances than edge sharing ones.

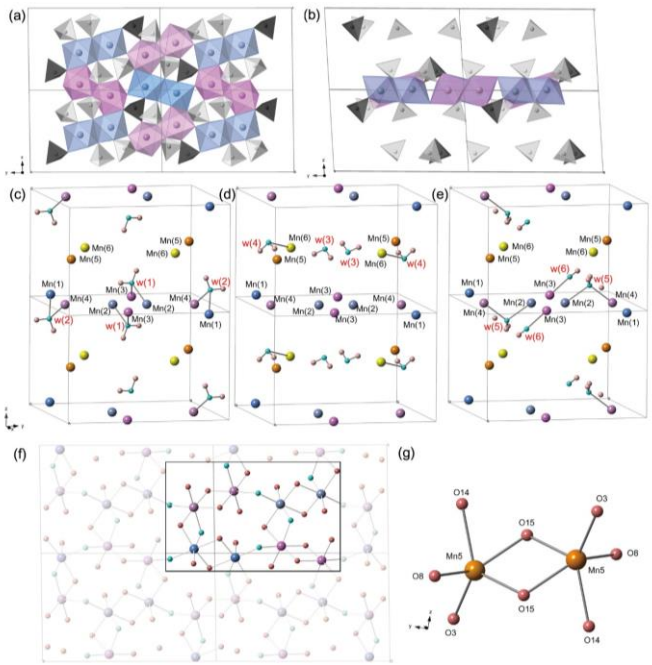

Figure 2. 4 (a, b) Crystal structure of $[Mn_4O_{10}(H_2O)_2]_2$ sheet composed of Mn(1), Mn(2), Mn(3), and Mn(4). Mn(5) and Mn(6) were omitted for clarity. (c) Chemical environment around water (1) and water (2) molecules. Water (1) were ligated to both Mn(2) and Mn(3) atoms, and water (2) were ligated to Mn(1) and Mn(4) atoms. (d) Chemical environment around water (3) and water (4). In the case of water (3), no chemical bond existed around water (3), while water (4) were solely ligated to Mn(6) atom. (e) Chemical environment around water (5) and water (6). Water (5) were ligated together with Mn(2) and Mn(4) atoms. Water (6) were only ligated to Mn(3) atoms. (f) Chemical structure of $[Mn_4O_{10}(H_2O)_2]_2$ unit cell. (g) Chemical structure of Mn_2O_8 dimer involving two Mn(5) atoms.

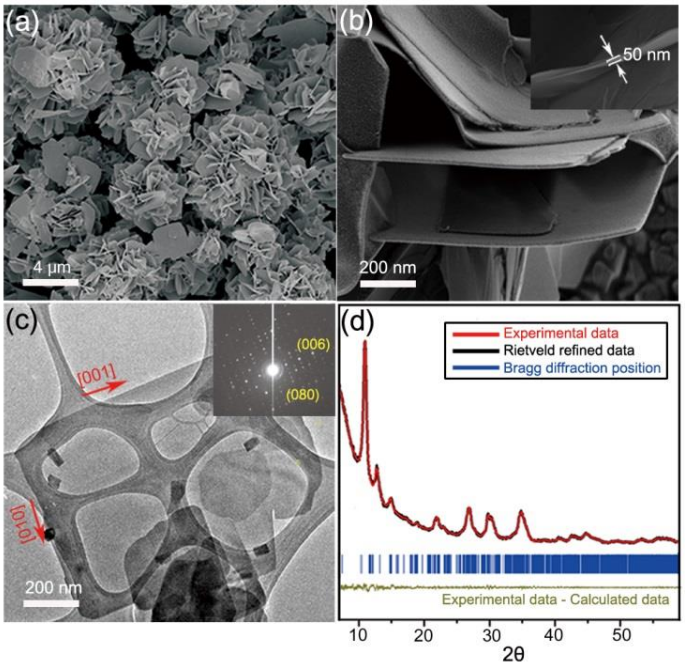

Figure 2. 5 Characterization of $Mn_3(PO_4)_2$-**3**H_2O. (a, b) SEM images and (c) TEM image of a [001], [010]-oriented $Mn_3(PO_4)_2$-**3**H_2O sheet and SAED patterns (inset). (d) Rietveld-refined XRD patterns of $Mn_3(PO_4)_2$-**3**H_2O. R_{wp} = 1.05%, R_p = 1.22%, R_{exp} = 0.59%, and χ^2 = 1.79.

2.2.2 Electrochemical analysis of $Mn_3(PO_4)_2$-$3H_2O$

The water oxidation catalytic characteristics of $Mn_3(PO_4)_2$-**3**H_2O were evaluated by cyclic voltammetry in 0.5 M sodium phosphate electrolyte at pH 7.(Figure 2.6) $Mn_3(PO_4)_2$-**3**H_2O was deposited on the FTO substrate using previously reported method.[80-81] The current value was normalized to the total weight or surface area of the catalyst on the working electrode. The OER activity curves were obtained by averaging the currents from the forward and reverse CV scans. (for raw CV curves before polarization correction, see Figure 2.7) Potentiostatic electrolysis of $Mn_3(PO_4)_2$-**3**H_2O yield a current value similar to the averaged one (Figure 2.8). We expected that the average current value could be a reasonable approximation of the true steady-state current. [80-81] As shown in Figure 2.6a, the oxygen evolution ability of $Mn_3(PO_4)_2$-**3**H_2O was higher than that of commercial MnO (99.99%) and MnO_2 (99.99%). The MnO and MnO_2 had monophasic features with high crystallinity (Figure 2.9).The current of $Mn_3(PO_4)_2$-**3**H_2O was 5.2 A g^{-1} whereas that of MnO and MnO_2 was both below 1 A g^{-1} at the overpotential value of 680 mV (Figure 2.6a). Even after normalization by the surface area of each catalyst, the OER current of $Mn_3(PO_4)_2$-$3H_2O$ (0.146 mA cm^{-2}_{cat}) was still much higher than that of MnO (0.063 mA cm^{-2}_{cat}) and MnO_2 (0.037 mA cm^{-2}_{cat}). The Tafel plot of each catalyst was obtained from polarization- corrected CV curves. The exchange current value of $Mn_3(PO_4)_2$-**3**H_2O was 3 times larger than that of MnO and MnO_2 (Figure 2.6b). The Tafel

slopes of $Mn_3(PO_4)_2$-$3H_2O$, MnO, and MnO_2 were shown to be around 120 mV/dec. It might be resulted from the existence of limitation on electron transport through the catalyst due to its low conductivity as observed similarly in poorly conductive metal oxide materials.[81] We are still investigating the catalytic performance of the carbon involved cell to improve its electrical conductivity.

In order to check the stability of the $Mn_3(PO_4)_2$-$\mathbf{3}H_2O$, we performed continuous potential cycling between 0.7 V and 1.5 V (vs NHE). As shown in Figure 2.8, the cyclic voltammetry currents of $Mn_3(PO_4)_2$-$\mathbf{3}H_2O$ remained nearly constant even after 100 cycles, indicating high catalytic durability of $Mn_3(PO_4)_2$-$\mathbf{3}H_2O$. HR-TEM analysis was performed to examine the phase stability of the $Mn_3(PO_4)_2$-$\mathbf{3}H_2O$ under OER condition. The single-crystalline feature of $Mn_3(PO_4)_2$-$\mathbf{3}H_2O$ was stably maintained after 30 min of bulk electrolysis at 1.5 V. (Figure 2.10)

We used gas chromatography to evaluate the properties of $Mn_3(PO_4)_2$-$3H_2O$, MnO, and MnO_2 as photochemical oxygen-evolving catalysts (Figure 2.11). Based on the amount of O_2 gas evolved during the initial 10 min of photolysis for each compound, the TOFs of the compounds were estimated. The TOF of $Mn_3(PO_4)_2$-$3H_2O$ was 0.024 μmol m^{-2} s^{-1}, which is higher than the TOF of MnO or MnO_2 (0.0084 μmol m^{-2} $s^{-1}$and 0.0077 μmol m^{-2} s^{-1}, respectively). Moreover, the TOF of $Mn_3(PO_4)_2$-$3H_2O$ (0.024 μmol m^{-2} s^{-1}) is higher than previously reported TOF values of Mn-oxide

catalysts (0.0055 - 0.017 μmol m^{-2} s^{-1}). In addition, the TOFs of the commercial MnO and MnO_2 used in this study were 0.0084 μmol m^{-2} $s^{-1}$and 0.0074 μmol m^{-2} s^{-1}, respectively, in agreement with pre-viously reported values for MnO_2 (0.0055 - 0.017 μmol m^{-2} s^{-1}). For comparison, the previously reported TOF values for other manganese compounds are summarized in Table 2.4.

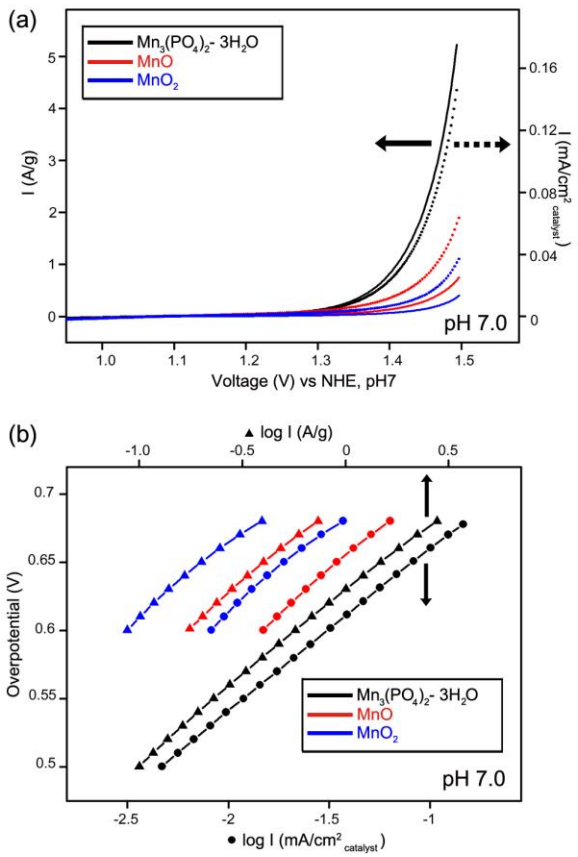

Figure 2. 6 Electrochemical characterization of $Mn_3(PO_4)_2$-$3H_2O$, MnO, and MnO_2. (a) Polarization-corrected cyclic voltammetry (CV) curves and (b) Tafel plots for $Mn_3(PO_4)_2$-$3H_2O$, MnO, and MnO_2 spin-coated on the FTO substrate in which the current value was normalized to the weight and surface area of the catalysts, respectively.

.

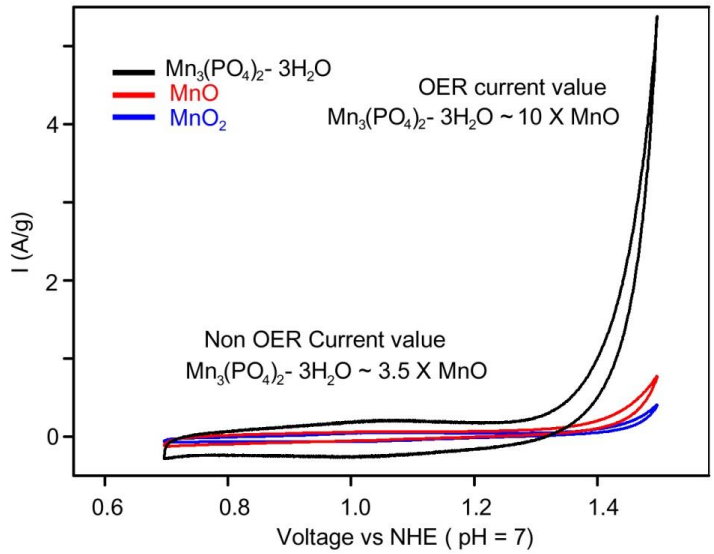

Figure 2. 7 Cyclic voltammetry curves for three catalysts before polarization correction : $Mn_3(PO_4)_2$-**3**H_2O (black), standard MnO (red) and MnO_2 (blue) Catalyst loaded working electrode was scanned at the rate of 10 mV sec^{-1} in 0.5 M phosphate buffer solution at applied potentials ranging from 0.7 V to 1.5 V. OER current of $Mn_3(PO_4)_2$-**3**H_2O was larger than that of MnO over 10 times at the applied voltage of 1.5 V (vs. NHE). Non OER current of $Mn_3(PO_4)_2$-**3**H_2O around 0.9 V which might be resulted from pseudocapacitive current was larger than that of MnO over 3 times. For obtaining particle surface area normalized CV curves, we used BET values of the catalysts. ($Mn_3(PO_4)_2$-**3**H_2O : 4.58 $m^2 g^{-1}$, MnO: 1.48 $m^2 g^{-1}$, MnO_2 : 1.69 $m^2 g^{-1}$).

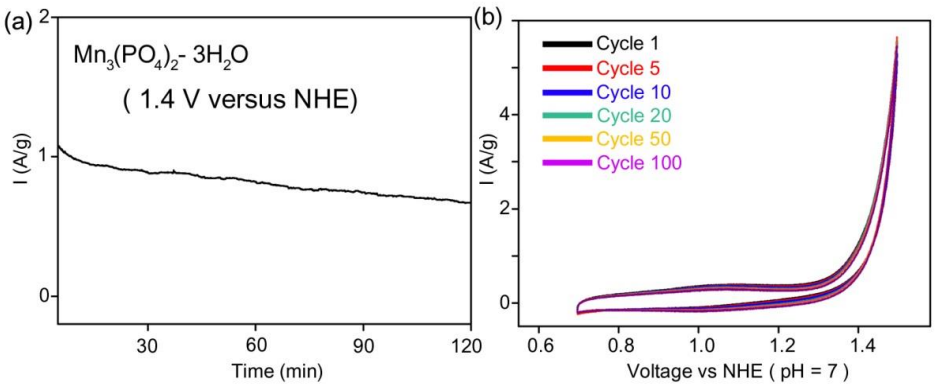

Figure 2. 8 (a) Catalytic current profile obtained upon constant potential (1.4 V vs NHE) electrolysis under pH 7. As shown in the figure, considerable catalytic current was maintained after 2 hours of electrolysis. (b) Cyclic Voltammetry curves of $Mn_3(PO_4)_2$-**3**H_2O, showing the 1^{st}, 5^{th}, 10^{th}, 20^{th}, 50^{th}, and 100^{th} cycles. All cyclic voltammetry curves were obtained in N_2 saturated 0.5 M Na-Pi buffer at a scan rate of 10 mV sec^{-1}.

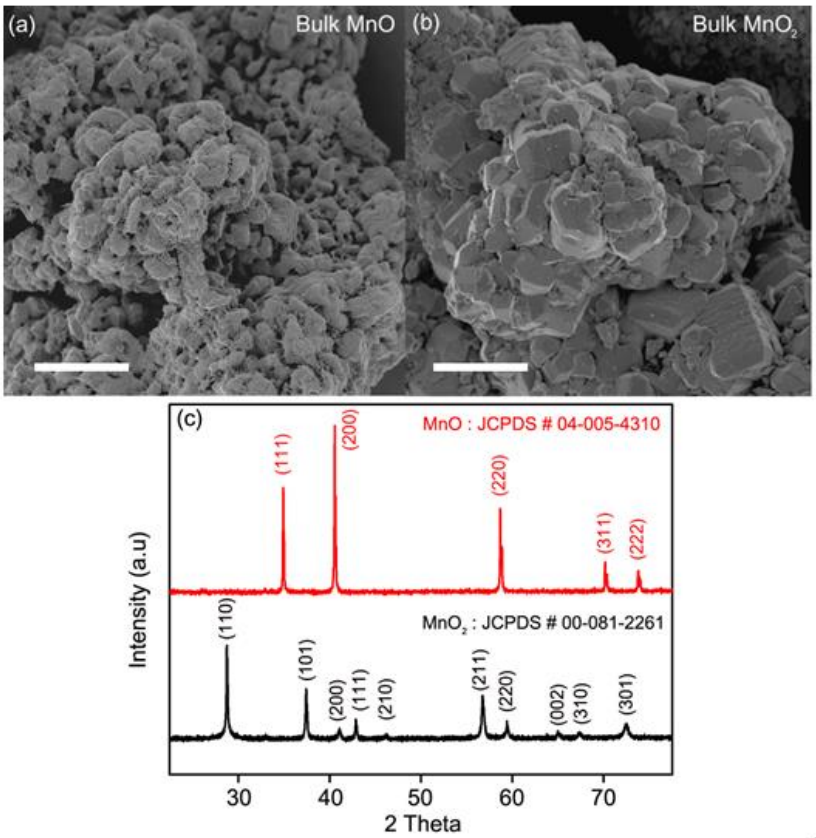

Figure 2. 9 FE-SEM images of (a) bulk MnO and (b) MnO_2. (c) The XRD patterns demonstrate that each material has monophasic features and that there are no secondary phases (scale bar: 10 μm)

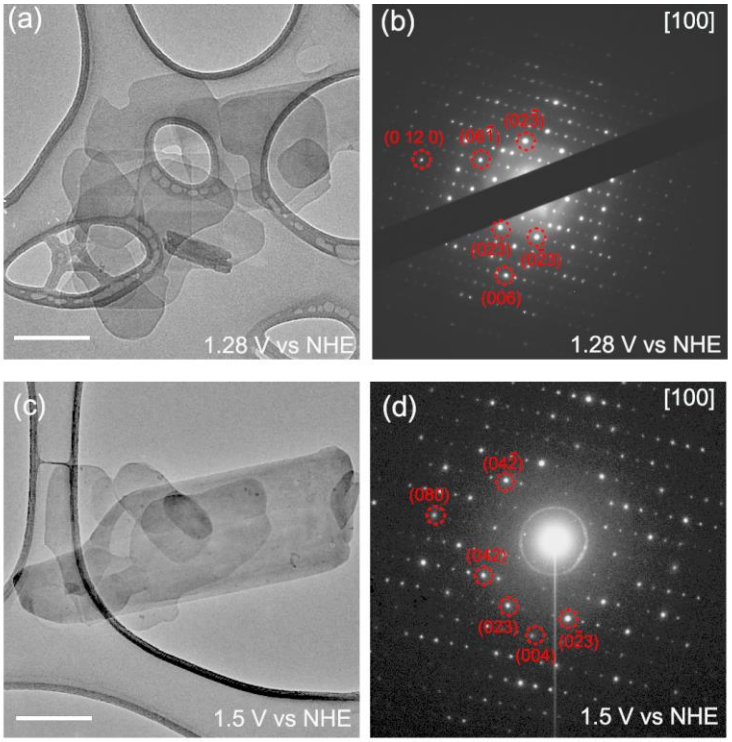

Figure 2. 10 Stability of $Mn_3(PO_4)_2$-$3H_2O$ during the water oxidation reaction. To evaluate the stability of $Mn_3(PO_4)_2$-$3H_2O$, bulk electrolysis analysis was performed at (a) 1.28 V and (c) 1.5 V. After 30 min of electrolysis, the catalysts were collected and analyzed. As shown in the SAED patterns, the single-crystalline feature of $Mn_3(PO_4)_2$-$3H_2O$ was maintained at both (b) 1.28 V and (d) 1.5 V (scale bar: 200 nm).

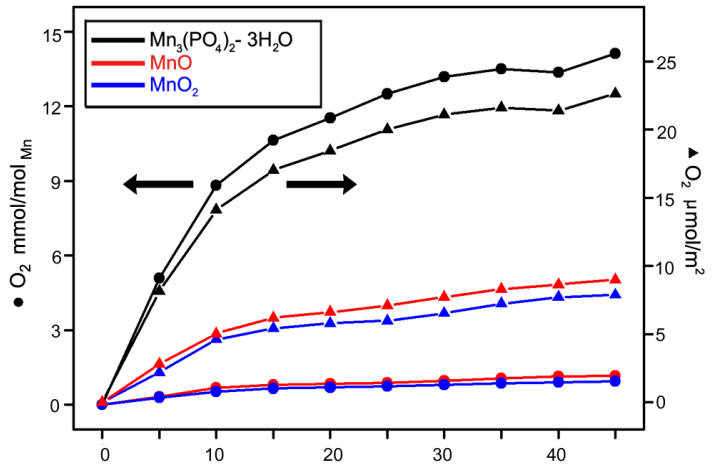

Figure 2. 11 The amount of oxygen evolved by $Mn_3(PO_4)_2$-$3H_2O$, MnO, and MnO_2 with a $Ru^{2+}(bpy)_3$–$S_2O_8^{2-}$ system, as recorded by gas chromatography (black, red, and blue). The amount of evolved oxygen was normalized to the total Mn atoms and surface area in the solution. The turnover frequency numbers of the compounds were estimated from the amount of oxygen gas evolved during the initial 10 min of photolysis for each compound.

Catalyst	**TOF (s^{-1} per Mn)**	**BET (m^2 per g)**	**TOF (μmol/m^2)**	**Experimental Condition**
λ-MnO_2(LT)	3.0 X 10^{-5}	20.0	0.017	
$CaMn_2O_4$	3.2 X 10^{-4}	303	0.0098	$Ru(bpy)_3Cl_2$ - $[Co(NH_3)_5Cl]Cl_2$, Acetate buffer (pH 4)
MnO_2 colloid	2.5 X 10^{-5}	40	0.0072	
α- MnO_2 nanotube	3.5 X 10^{-5}	25.1	0.016	$Ru(bpy)_3Cl_2$ - $Na_2S_2O_8$,No buffer (Initial pH 7)
α- MnO_2 nanowire	5.9 X 10^{-5}	47.9	0.014	$Ru(bpy)_3Cl_2$ - $Na_2S_2O_8$,No buffer (Initial pH 7)
β- MnO_2 nanowire	2.0 X 10^{-5}	14.9	0.015	$Ru(bpy)_3Cl_2$ - $Na_2S_2O_8$,No buffer (Initial pH 7)
Bulk α- MnO_2	1.0 X 10^{-5}	20.8	0.0055	$Ru(bpy)_3Cl_2$ - $Na_2S_2O_8$,No

				buffer (Initial pH 7)
Our catalyst	1.5 X 10^{-5}	4.58	0.024	$Ru(bpy)_3Cl_2$ - $Na_2S_2O_8$, 0.1 M Na- Pi buffer (pH 7)
MnO_2 (commercial)	1.1 X 10^{-6}	1.48	0.0077	
MnO (Commercial)	8.8 X 10^{-7}	1.69	0.0084	

Table 2. 4 The TOF values of the various manganese oxide catalysts that have been reported[51-55] and of our catalyst, commercial MnO, and MnO_2, which were used in this study for water oxidation catalysis. TOF values (s^{-1} per Mn, μmol/m^2 s) were calculated based on the oxygen evolution rates divided by the mole number of Mn atoms and total surface area of the catalysts. These values are indexed in the second and fourth columns, respectively. The BET values of the catalysts and the experimental conditions are summarized in the third and fourth columns, respectively.

2.2.3 Mechanistic studies of $Mn_3(PO_4)_2$-$3H_2O$

The electron paramagnetic resonance (EPR) spectroscopy was utilized to investigate the manganese oxidation state of the $Mn_3(PO_4)_2$-$3H_2O$. Three potentials (1.0 V, 1.28 V and 1.40 V) were selected to investigate the effect of changing potential on the manganese oxidation state during the catalytic cycle. The perpendicular mode continuous-wave EPR (CW-EPR) spectra of $Mn_3(PO_4)_2$-$3H_2O$ at three different applied potentials are shown in Figure 2.12a. The EPR spectrum of as-prepared $Mn_3(PO_4)_2$-$3H_2O$ exhibits a characteristic S = 5/2, Mn^{II} signal, at g ~2 with a six-line ^{55}Mn (I = 5/2, 100% abundance) hyperfine splitting. Up to the electrolysis potential of 1.4 V, EPR spectra feature of Mn^{II} was maintained irrespective of applied potential values. We tried to detect other manganese oxidation state, Mn^{III},with parallel polarization EPR using previous method1[82], but only observed a broad peak arising most likely from oxygen due to the fast decaying nature of Mn^{III} (Figure 2.13). We then prepared the samples in pyrophosphate solution, which has been shown to effectively ligate to Mn^{III} ions before decaying and also known as redox-inert agent[83]. Figure 2.12b presents the parallel-mode CW-EPR at different applied potentials. The well-resolved six-line S = 2, Mn^{III} signal which cannot be detected from as-prepared $Mn_3(PO_4)_2$-$3H_2O$ powder,

with hyperfine coupling of ~ 42 G centered at g_{eff} ~ 8.2, appeared. This result shows the existence of Mn^{III} species on the surface of $Mn_3(PO_4)_2$-$3H_2O$ under OER condition.[62, 84]

To obtain a microscopic understanding of the improved catalytic activity of manganese phosphate, we performed DFT calculations and determined how much J-T distortion is induced for the Mn^{III} configuration, which is an important criterion for the stability of the Mn^{III} state. First, we selected β-MnO_2, which is composed of the highly symmetric MnO_6 octahedron.[85] According to a recently proposed mechanism [57], the surface oxidation state of β-MnO_2 is spontaneously reduced to Mn^{II} by electron injection from H_2O and then electro-oxidized into Mn^{III} when an electric potential of ~1.5 V with respect to NHE is applied. Thus, we first negatively charged β-MnO_2 by adding a number of electrons to enforce the Mn^{II} state in β-MnO_2 ($Mn^{IV} \rightarrow Mn^{II}$) and then oxidized this negatively charged β-MnO_2 to form Mn^{III} ($Mn^{II} \rightarrow Mn^{III}$). The pair distribution function shows that the average distance of Mn-O is 1.916Å , which splits into 1.840 and 1.916 Å as a result of oxidation of Mn^{II} to Mn^{III} (Figure 2.14a). This small splitting indicates that the J-T distortion is significantly hindered.

However, the rate-limiting step in the catalytic cycle of $Mn_3(PO_4)_2$-$3H_2O$ is not yet fully resolved. Nevertheless, the transition from Mn^{II} to Mn^{III} is likely an important step [57], as in other Mn^{II}-based OER catalysts. In fact, the existence of Mn^{III} during the catalytic cycle was confirmed by EPR. For

theoretical investigation, therefore, we positively charged $Mn_3(PO_4)_2$-**3**H_2O by reducing a number of electrons such that all the Mn atoms were converted from Mn^{II} to Mn^{III}. The resulting pair distribution function of Mn-O in Figure 2.14b demonstrates that the Mn-O bond lengths are split into various values of 1.980-2.524 Å upon full oxidation, clearly demonstrating significant J-T distortion in the Mn^{III} octahedra of up to 0.5 Å.

We also performed similar calculations for MnO, which has the same resting Mn valency (Figure 2.14c). The Mn^{II}-O bond length (2.240 Å on average) splits into 2.090 and 2.440 Å in the Mn^{III} configuration, indicating a degree of J-T distortion similar to that observed for $Mn_3(PO_4)_2$-**3**H_2O.

As another standard to gauge the stability of Mn^{III}, we examined the average pressure when all the Mn atoms were in the Mn^{III} configuration (Figure 2.14 d). A large value of pressure implies a tendency for the lattice to be distorted and destabilized when Mn^{III} atoms are abundant. As shown in Figure 2.14 d, the magnitude of pressure follows the order MnO_2 > MnO > $Mn_3(PO_4)_2$-**3**H_2O. Interestingly, the catalytic activity in Figure 2.6a exactly follows the reverse order. Therefore, in combination with the above analysis of the J-T distortion, we conclude that the structural flexibility that stabilizes the Mn^{III} state is the key property underlying the high catalytic activity of $Mn_3(PO_4)_2$-**3**H_2O.

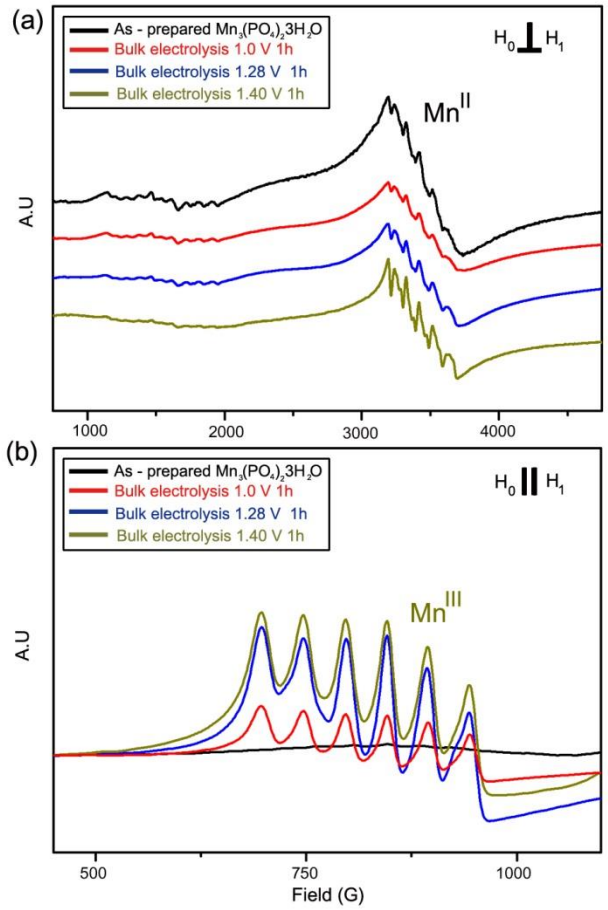

Figure 2. 12 EPR analysis of $Mn_3(PO_4)_2$-$3H_2O$, showing the valence change of Mn. (a) Perpendicular mode and (b) Parallel mode X-band CW-EPR spectra of $Mn_3(PO_4)_2$-$3H_2O$ varying electrolysis potentials with constant bulk electrolysis time of 1 hr.

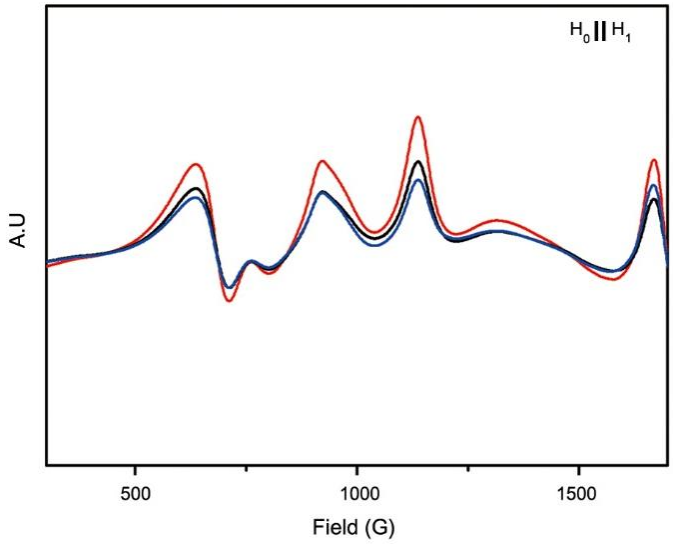

Figure 2. 13 Parallel mode CW-EPR Spectra of $Mn_3(PO_4)_2$-**3**H_2O at three different potentials, 1.0 V (blue), 1.28 V(black), 1.40 V(red) respectively. When the stabilizing agent, pyrophosphate was not used during the preparation of EPR samples, Mn^{III} hyperfine splitting was not observed but only broad signal arising from oxygen were detected.

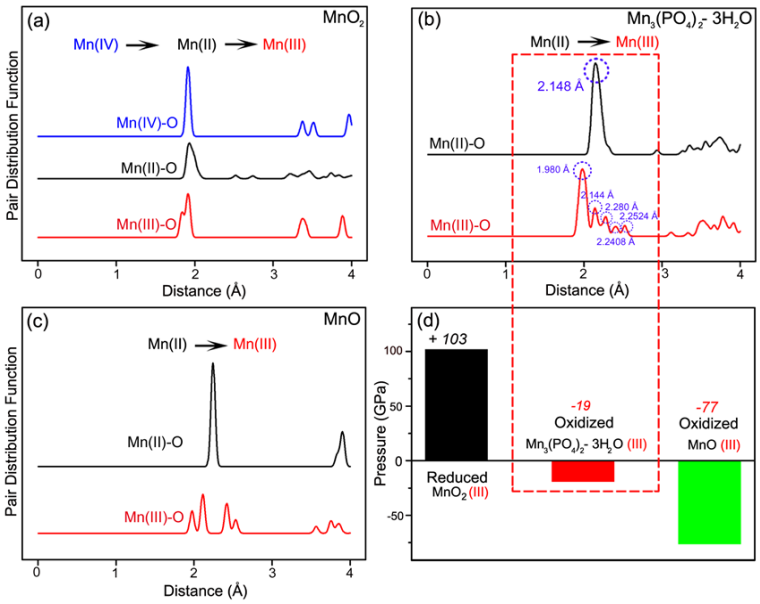

Figure 2. 14 The pair distribution functions of manganese atoms (a) in pristine MnO_2 (blue) and reduced manganese oxide as Mn(II) (black) and Mn(III) (red); (b) in pristine $Mn_3(PO_4)_2$-$3H_2O$ (black) and oxidized manganese phosphate (red) in which all Mn^{II} atoms were intentionally oxidized to Mn^{III}; and (c) in pristine MnO (black) and oxidized manganese oxide (red). The pair distribution function near 2 Å in $Mn_3(PO_4)_2$-$3H_2O$ indicates that the Mn-O bonds originated from phosphate groups. In contrast to MnO_2, the split of the pair distribution function from black to red in $Mn_3(PO_4)_2$-$3H_2O$ and MnO indicates the J-T distortion. (d) The pressure on the cell of each Mn compound when Mn was reduced or oxidized to the 3+ state.

Chapter 3. $Li_{2-x}MnP_2O_7$ (x = 0 ~ 1)

: Effect on Mn Valency on OER catalysis

3.1 Experimental and Procedure

3.1.1 Synthesis and Materials

$Li_2MnP_2O_7$ samples were prepared using conventional solid-state synthesis using stoichiometric mixture of Li_2CO_3 (ACS reagent, ≥99%, Aldrich), MnC_2O_4 (≥99%, Alfa Aesar), and $(NH_4)_2HPO_4$ (ACS reagent 98%, Aldrich). These precursors were mixed by ball milling for 12 h. The precursor mixture was initially heated at 300 ℃ for 6 h under steady Ar flow. The calcined sample was pelletized using a disk-shaped mold, and calcined again at 600 ℃ for 10 h under steady Ar flow.

To prepare $Li_{2-x}MnP_2O_7$, $Li_2MnP_2O_7$ was chemically delithiated using NO_2BF_4 (Aldrich, 95%) in acetonitrile solvents (99%, Aldrich) according to the following reaction :

$$Li_2MnP_2O_7 + x\ NO_2BF_4 \rightarrow Li_{2-x}MnP_2O_7 + x\ LiBF_4 + x\ NO_2$$

NO_2BF_4 was used as a strong oxidizing agent with a redox potential for

NO_2^+/NO_2 of 5.1 V versus Li^+/Li.[74] The final product, $Li_{2-x}MnP_2O_7$, was obtained by washing the reactants several times with acetonitrile.

3.1.2 Characterization

3.1.2.1 ICP/MS

Inductively coupled plasma-mass spectrometer (ICP/MS, 720-ES, Varian) measurements were conducted to determine the exact chemical composition of the $Li_{2-x}MnP_2O_7$ (x=0, 0.3, 0.5, 1) nanoparticles.

3.1.2.2 Powder X-ray diffraction, Full-pattern matching

Powder X-ray diffraction (XRD) was performed on a D-8 Advance X-ray diffractometer with Cu Kα radiation (λ=1.54056 Å). XRD patterns were recorded in a range of 10-80° with a step size of 0.01°. The resulting XRD patterns were compared with previously reported one.[75]

Rietveld refinement was performed using TOPAS Academic. The crystal structure of $Li_{2-x}MnP_2O_7$ was drawn with VESTA program based on its atomic coordination information. The maximum bond length between manganese atom and oxygen atom was set to 2.6 Å .

3.1.2.3 X-ray photon spectroscopy (XPS)

X-ray photo-electron spectroscopy (XPS) spectra were obtained by electron spectroscopy (Sigma Probe; Thermo VG Scientific, UK) with a pass energy of 30 eV and a step size of 0.1 eV. All the binding energies are referenced to C 1s (284.5 eV).

3.1.2.4 Transmission electron microscopy(TEM) analysis

TEM images and selected area electron diffraction (SAED) patterns were obtained using a high resolution transmission electron microscope (JEM-3000F, JEOL, Japan) with an acceleration voltage of 300 kV. The TEM samples were collected from as-prepared compounds or from FTO glass directly following the electrochemical measurement and were dispersed in ethanol by sonication for approximately 5 min. Approximately 10 μl of dispersed $Li_{2-x}MnP_2O_7$ was dropped on the lacy carbon TEM grid and air-dried and then further dried in a vacuum oven at 70 ℃ for 30 min to evaporate the solvent.

3.1.2.5 Brunauer–Emmett–Teller (BET) method

Brunauer-Emmett-Teller (BET) analysis was conducted on the Li_{2-}

$_xMnP_2O_7$ (x=0, 0.3, 0.5, 1) compounds, MnO, and MnO_2. In total, 0.5070 g of the sample was loaded in the BET analyzer (Physisorption Analyzer, Micromeritics, USA) under an N_2 adsorption environment.

3.1.3 Electrochemical analysis

3.1.3.1 Cyclic Voltammetry (CV)

All the electrochemical experiments were conducted in a three-electrode electrochemical cell system. A BASi Ag/AgCl/3M NaCl reference electrode and Pt foil (2 cm X 2 cm X 0.1 mm, 99.997% purity, Alfa Aesar) were used as the reference electrode and counter electrode, respectively. The electrochemical tests were performed at ambient temperature (21 ± 1℃) using a potentiostat system (CHI 760C, CH Instruments, Inc.). The electrode potential was converted to the NHE scale using the following equation: E(NHE) = E(Ag/AgCl) + 0.197 V. Additionally, the overpotential values were calculated from the difference between the iR corrected potential ($V = V_{applied} – iR$) and the thermodynamic point of water oxidation at a specified pH. The electrolyte was a phosphate buffer with a designed buffer strength under pH 7.0. The electrolyte was degassed by bubbling with high-purity nitrogen (99.999%) for at least 1 hour before the start of each experiment.

The preparation procedure of the working electrodes containing our catalysts can be described as follows. First, 5 mg of the catalyst powder was dispersed in 1 ml of deionized water mixed with 100 μl of neutralized Nafion solution. Then, the mixture was sonicated for at least 30 min to produce homogeneous ink. Next, 50 μl of the catalyst solution was dropped onto the FTO substrate, and spin-coating was performed at 2000 rpm for 30 sec. Finally, the prepared working electrode was dried in an 80 ℃ oven for 5 min before the CV measurements. The weight of the catalyst onto the FTO substrate was carefully measured by a micro weighing electronic scale (Sartorius Micro Balance). Before every electrochemical experiment, the solution resistance was measured in the electrolysis bath. All the data were iR-compensated. For the stability test, the working electrode was cycled 100 times, with the potential range from 0.7 V to 1.5 V versus NHE at a scan rate of 10 mV/sec.

3.1.4 DFT calculation

The first principles calculations were conducted to determine the energies of given structures, based on spin-polarized generalized gradient approximation (GGA) using Perdew-Burke-Ernzerhof (PBE) exchange-correlation parameterization and density functional theory (DFT). We applied the Hubbard parameter (GGA+U) to correct the incomplete cancelation of the self-interaction of GGA. Ab initio quantum mechanical calculation was performed with the Vienna ab initio simulation package (VASP) using the projector-augmented wave (PAW) method. A plane-wave basis with an energy cutoff was 500 eV and appropriate k-point meshes were sampled by a 2×2×2 monkhorst-pack mesh. All structures are fully relaxed. The atomic charges were calculated by the Voronoi spin integration.

3.2 Results and Discussions

3.2.1 Structural Characterization of $Li_{2-x}MnP_2O_7$ (x=0~1)

A $Li_2MnP_2O_7$ compound was synthesized using a previously reported conventional solid-state method. A stoichiometric amount of Li_2CO_3, $MnC_2O_4 \cdot 2H_2O$, and $(NH_4)_2HPO_4$ was initially mixed by planetary milling for 12 h. Then, the mixture was initially heated at 300 ℃ for 6 h, and heated again at 600 ℃ for 10 hours under steady Ar flow to produce the $Li_2MnP_2O_7$ compound. The XRD pattern of the synthesized compound matches well with the previously reported pattern of $Li_2MnP_2O_7$ (Figure 3.1a). Close observation of the $Li_2MnP_2O_7$ crystal allows us to distinguish two different manganese sites in one unit cell; one is trigonal bipyramidal (TBP) (MnO_5), and the other is octahedral (Oh) (MnO_6). The TBP and Oh polyhedrons formed M_2O_9 sub-units by edge-sharing coordination. As illustrated in Figure 3.1b, the surrounding geometry of each manganese atom is symmetrically broken, and the M_2O_9 sub-units are interconnected through bulky P_2O_7 groups to form the three-dimensional framework structures. The asymmetric geometry of each manganese atom can be clearly observed by measuring the distances and angles between the manganese and oxygen atoms. The TBP polyhedron has various O-Mn-O angles and Mn-O distances ranging from 82.61° to 152.17° and from 2.117 Å to 2.246 Å, respectively. The Oh polyhedron also

exhibits an asymmetric geometry, with the O-Mn-O angles and Mn-O distances ranging from 82.47° to 110.65° and from 2.119 Å to 2.308 Å, respectively. Additionally, the shortest Mn-Mn distance is 3.302 Å and the second shortest Mn-Mn distance is 5.010 Å which are longer than any other manganese oxides due to the bulky P_2O_7 groups that interconnects manganese polyhedrons.

To understand the effect of Mn valency on the OER, we attained $LiMnP_2O_7$, $Li_{1.5}MnP_2O_7$, and $Li_{1.7}MnP_2O_7$ compounds by removing Li^+ ions from $Li_2MnP_2O_7$ powders. $Li_2MnP_2O_7$ was chemically delithiated using NO_2BF_4 according to the following reaction:

$$Li_2MnP_2O_7 + xNO_2BF_4 \rightarrow Li_{2-x}MnP_2O_7 + xLiBF_4 + xNO_2.$$

NO_2BF_4 was used as a strong oxidizing agent with a redox potential for NO_2^+/NO_2 of 2.05 V versus NHE (5.1 V versus Li^+/Li.)[74] As the amount of NO_2BF_4 increased, the averaged Mn valency in $Li_{2-x}MnP_2O_7$ gradually changed from 2 to 3. There was no significant change in the morphology, size or surface area arising from the delithiation, as observed by TEM and BET analysis

XRD, XPS, and ex-situ XANES (X-ray absorption near-edge structure) analysis of $Li_{2-x}MnP_2O_7$ (x = 0, 0.3, 0.5, 1) was performed to probe the gradual delithiation and change in Mn valency. The delithiation process in $Li_2MnP_2O_7$ proceeds in a monophasic manner, accompanying a continuous

peak shift without any appearance or disappearance of the peak (Figure 3.2a and inset). For example, the (110) peak continuously shifts from 14.10° to 14.01°, and the (002) peak also shifts from 16.27° to 16.18°. Each XRD pattern was analyzed by full pattern matching, and the corresponding lattices were refined. The variation of the lattice parameter and unit cell volume as a function of Li content in $Li_{2-x}MnP_2O_7$ (x = 0 ~ 1) is demonstrated in Figure 3.2 b. During the delithiation process, the lattice parameters and unit-cell volume expand. However, it should be noted that the change is only ~ 1%, which implies the minimal change in the overall crystal structure. *Ex-situ* XANES Mn K-edge spectra of $Li_{2-x}MnP_2O_7$ (x = 0, 0.3, 0.5, 1) powders shift toward a higher energy as more Li ions removed from $Li_2MnP_2O_7$, indicating the gradual oxidation of averaged oxidation state of Mn from 2 to 3 along the delithiation (Figure 3.3a). Additionally, XPS was used to probe the Mn oxidation state at the surface and for 2 nm-etched surfaces of $Li_{2-x}MnP_2O_7$ (x = 0, 0.3, 0.5, 1) by comparing the relative position of the Mn $2p_{1/2}$ peak. In both the surface and 2 nm-etched surfaces of the catalysts, the binding energy of the Mn $2p_{1/2}$ peak increases gradually from 653.2 eV to 654.5 eV as the Li ion content decreases, confirming the gradual oxidation of Mn upon delithiation (Figure 3.3b).

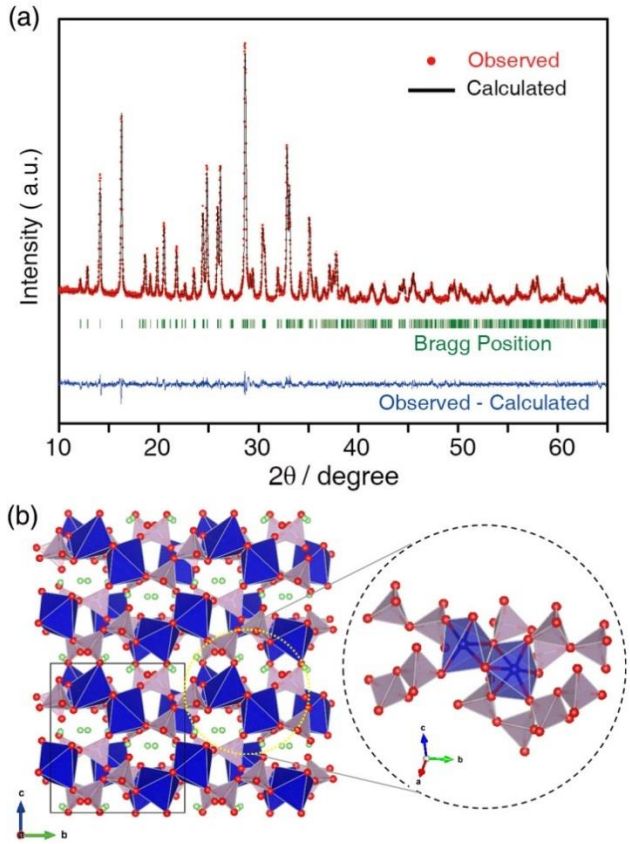

Figure 3. 1 (a) Rietveld refinement pattern of high-resolution X-ray diffraction data for $Li_2MnP_2O_7$. Red dots (experimental data points), the black line (calculated powder pattern), the green ticks (Bragg positions), and the blue line (difference between the observed and calculated patterns). R_P=1.59 %, R_{WP}= 2.07 %, R_I= 0.956 %, R_F= 1.22 %, χ^2=2.11 (b) Crystal structure of $Li_2MnP_2O_7$. Inset shows the local environment around the Mn_2O_9 sub-unit (blue). The pyrophosphate units and Li atoms are depicted in gray and green, respectively.

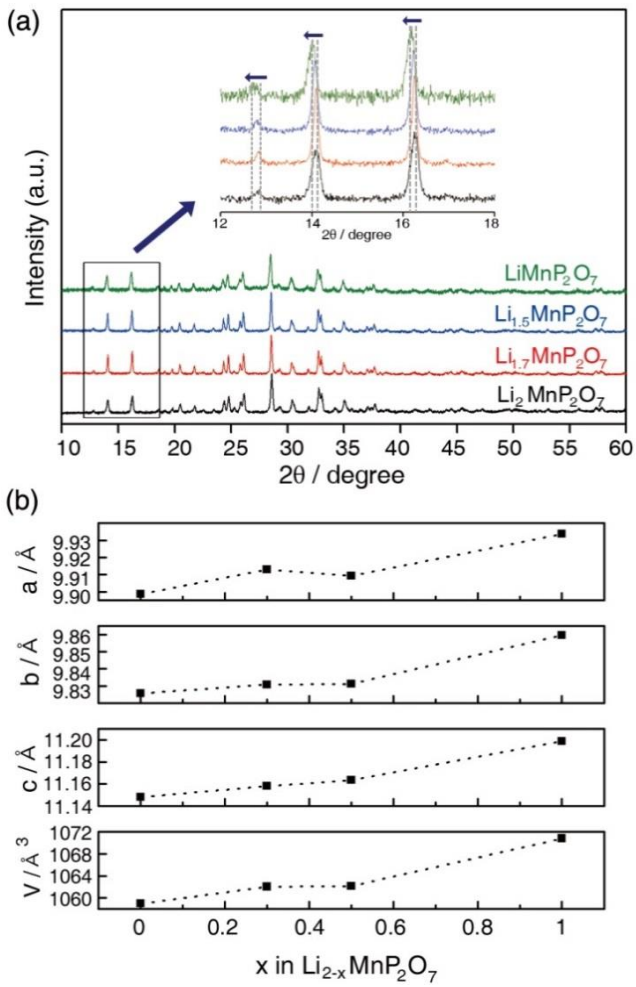

Figure 3. 2 (a) Powder XRD patterns of $Li_2MnP_2O_7$ (black), $Li_{1.7}MnP_2O_7$ (red), $Li_{1.5}MnP_2O_7$ (blue), and $LiMnP_2O_7$ (green). The inset reveals the gradual peak shift during delithiation. (b) The change in the lattice parameters, as determined by Rietveld refinement, and the corresponding unit-cell volumes as a function of Li content in $Li_{2-x}MnP_2O_7$ (x=0.0-1.0).

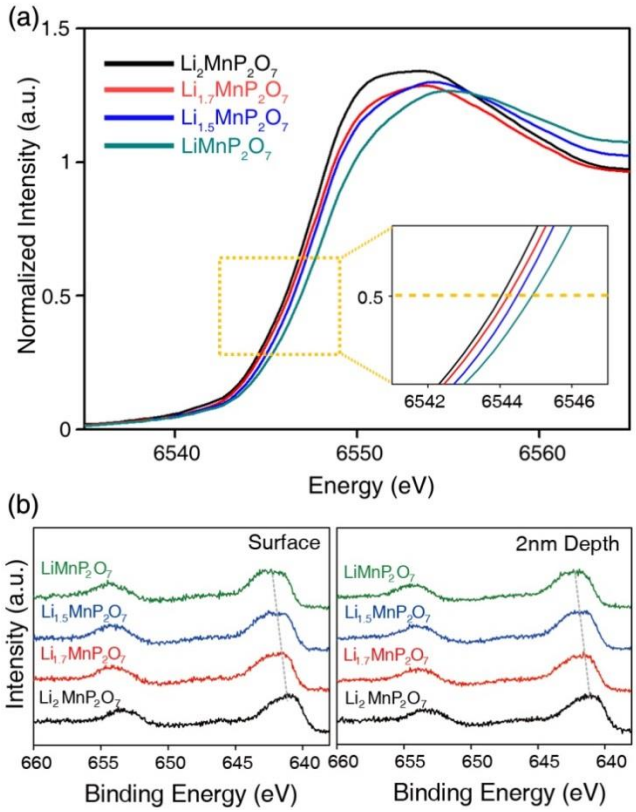

Figure 3. 3(a) *Ex-situ* XANES Mn K-edge spectra of $Li_{2-x}MnP_2O_7$ (x = 0, 0.3, 0.5, 1) powders. Inset shows gradual oxidation Mn atoms in $Li_{2-x}MnP_2O_7$ (x = 0, 0.3, 0.5, 1) along the delithiation. (b) XPS spectra of the Mn 2p region of $Li_2MnP_2O_7$ (black), $Li_{1.7}MnP_2O_7$ (red), $Li_{1.5}MnP_2O_7$ (blue), and $LiMnP_2O_7$ (green) at the surface (left) and for a 2 nm-etched surface (right).

3.2.2 Electrochemical analysis of $Li_{2-x}MnP_2O_7$ (x=0~1)

The water oxidation catalytic properties of $Li_{2-x}MnP_2O_7$ (x = 0, 0.3, 0.5, 1) were evaluated by cyclic voltammetry under neutral conditions (500 mM sodium phosphate buffer, pH 7.0). (Figure 3.4 and Figure 3.5) Working electrodes were prepared by spin-coating a suspension of catalyst in Nafion solutions onto a FTO (fluorine-doped tin oxide) substrate using a previously reported method.[80-81] The current value was normalized by the total weight or surface area of the catalyst on the working electrode. The total surface area of the catalysts onto the substrate was estimated by multiplying the BET (m^2/g) values and the weight of the catalysts (g) onto the substrate. For correction of the polarization current, we obtained OER curves by averaging the currents from the forward and reverse CV scans. Potentiostatic electrolysis of $Li_{2-x}MnP_2O_7$ (x=0, 0.3, 0.5, and 1) results in a similar current value as the averaged one (Figure 3.6). This finding indicates that the averaged current could be a reasonable approximation of the true steady-state current. [80-81] Interestingly, we observed that the oxygen evolution ability is enhanced as the averaged Mn oxidation state of as-prepared catalysts ($Li_{2-x}MnP_2O_7$) increases from 2 to 3. As shown in Figure 3.4, the current density of $LiMnP_2O_7$ (5.0 A/g at the overpotential value of 680 mV), in which all the Mn atoms have a trivalent oxidation state, was 2.5 times larger than that of $Li_2MnP_2O_7$ (2.0 A/g at the over potential value of 680 mV), which has only divalent Mn atoms. The current values at the overpotential of 680 mV for $Li_{1.5}MnP_2O_7$ and

$Li_{1.7}MnP_2O_7$ were 4.0 A/g, and 2.8 A/g, respectively. The enhanced catalytic ability of $Li_{2-x}MnP_2O_7$ upon delithiation was also observed when we normalized the current value to the total surface area of the catalyst (Figure 3.4). We also conducted the same experiments for commercially available MnO (purity 99.99%) and MnO_2 (purity 99.99%) for comparison (Figure 3.7). The current values of MnO and MnO_2 at the overpotential value of 680 mV are 0.75 A/g and 0.36 A/g,respectively (Figure 3.7). When we normalized the current value to the total surface area of the catalyst, the current density of MnO and MnO_2 are to 64 $\mu A\ cm^{-2}$ and 34 $\mu A\ cm^{-2}$ which corresponds well with the previous reports (Figure 3.7).[57] According to previous study, the current density of δ-MnO_2 was ~ 40 $\mu A\ cm^{-2}$ at the overpotential value of 680 mV at pH 7. The current density of $LiMnP_2O_7$ is approximately 6.5 times and 14 times higher than that of MnO and MnO_2, respectively. Moreover, $Li_2MnP_2O_7$ displayed a higher current density than that of MnO_2 and MnO by 6.0 times and 2.5 times, respectively.

A Tafel plot of each catalyst was obtained from steady-state current measurement in which the current was normalized to the total surface area of the catalyst. The steady-state currents were averaged and the variations in the currents were indicated with error bars. As shown in Figure 3.5, the exchange current value increased in the series $Li_2MnP_2O_7 < Li_{1.7}MnP_2O_7 < Li_{1.5}MnP_2O_7 < LiMnP_2O_7$. The slopes of all the $Li_{2-x}MnP_2O_7$ (x = 0, 0.3, 0.5, 1) samples, MnO and MnO_2 were measured to be ~ 120 mV/decade.

In order to check the catalytic stabilities of the $Li_{2-x}MnP_2O_7$ compounds under OER conditions, we performed subsequent potential cycling from 0.7 V to 1.5 V versus NHE in 0.5 M sodium phosphate buffer at pH 7.0. The OER and pseudocapacitive currents of $Li_2MnP_2O_7$ and $LiMnP_2O_7$ remained nearly constant, even after 100 cycles, during voltammetry cycling (Figure 3.8 and Figure 3.9). $Li_{1.7}MnP_2O_7$ and $Li_{1.5}MnP_2O_7$ also did not exhibit any noticeable change in their currents during voltammetry cycling indicating their high catalytic stability (Figure 3.10). Moreover, for verifying whether surface area of the $Li_2MnP_2O_7$ remains constant during the OER, we compared the pseudocapacitive charge storage of $Li_2MnP_2O_7$ during the CV scans. According to previous reports[86-88], the shaded area during the CV in Figure 3.11 can be estimated to be proportional to the cathodic charge. In our case, the shaded areas of both 1st cycle and 100th cycle of $Li_2MnP_2O_7$ normalized to their initial weight onto the FTO substrate show almost identical indicating the surface area of the $Li_2MnP_2O_7$ remains nearly constant during the OER. Tafel plots of $Li_2MnP_2O_7$ and $LiMnP_2O_7$ in several selected cycles were demonstrated to be almost constant, with a slope value of ~120 mV/decade (Figure 3.9 a, b inset).

In order to observe whether Li ions can be leached out during the OER and confirm the stability of all the catalysts, we performed XPS, ICP, and *ex-situ* XANES analysis. We applied 1.5 V vs NHE for 3hrs in 0.5 M sodium phosphate buffer at pH 7.0 for each catalysts. First, using XPS, we compared the binding energy of the Mn $2p_{1/2}$ peaks of as-prepared samples

(before OER) and bulk-electrolyzed samples (after OER). Even after 3 hrs of bulk electrolysis, the peak position of the Mn $2p_{1/2}$ remained unchanged compared to the as-prepared samples (Figure 3.12). Since XPS measurement is especially surface-sensitive, the invariance of XPS Mn peak strongly supports that the oxidation states of Mn both at the bulk and the surface was maintained without any leaching effect of the Li ion during OER. Moreover, ICP analysis for the catalysts clearly shows that the ratio of Li ions to Mn ions remained the same after electrolysis (Table 3.1). For example, the ratio of Mn to Li ions of $Li_2MnP_2O_7$ of $LiMnP_2O_7$ after electrolysis were 1.99 and 0.99, respectively, indicating no delithiation occurs during OER. Additionally, Li ion could not be detected in the electrolyte solution after the bulk electrolysis using ICP analysis. Furthermore, to clearly observe the possible change in oxidation state of Mn resulted from the delithiation during the OER, we performed *Ex-situ* XANES(X-ray absorption near-edge structure) analysis. *Ex-situ* XANES corresponding to Mn K-edge spectra of as-prepared and bulk-electrolyzed $Li_2MnP_2O_7$ were same indicating oxidation state of Mn ions inside the crystal was maintained during the OER (Figure 3.12). This result further supports that delithiation did not occur during the OER. If some portion of Li ion was removed during the OER, Mn K-edge spectra of electrolyzed $Li_2MnP_2O_7$ shifted toward the higher energy region than that of as-prepared $Li_2MnP_2O_7$.

Additionally, in order to verify the delithiation of our $Li_2MnP_2O_7$ powders did not occur up to the highest applied potential in our study (1.5 V

vs NHE) at the room temperature, we conducted cyclic voltammetry and charging-discharging measurement of the powders in a practical battery setup. Briefly, the cathode was formulated by mixing 75 wt% $Li_2MnP_2O_7$ and 20 wt% Super P carbon black and 5 wt% polyvinylidene fluoride (PVDF) binder with a minimal amount of N-methylpyrrolidone. Galvanostatic charge-discharge cycling was conducted in the voltage range from 2 to 4.55 V at a rate of C/20. However, it showed negligibly low capacity during charge and discharge which is well matched with the previous report [89] (Figure 3.13). Additionally, after voltage cycling of $Li_2MnP_2O_7$ in a practical battery setup, we performed *ex-situ* XANES analysis of cycled $Li_2MnP_2O_7$ obtained from the electrochemical coin cell. *Ex-situ* XANES corresponding to Mn K-edge spectra of cycled $Li_2MnP_2O_7$ and as-prepared $Li_2MnP_2O_7$ which is also obtained from the coin cell before cycling show no difference further supporting delithiation does not occur during the OER even after mixing the catalyst with carbon (Figure 3.13 inset). We applied potential cycling from 3.75 V to 4.55 V vs Li/Li^+ scale (0.7 V to 1.5 V vs NHE) which is identical to the voltage range during the OER in our study. However, we found no distinct reversible cathodic and anodic peaks which can be resulted from the delithiation/lithiation of the $Li_2MnP_2O_7$ (Figure 3.13b). The current profile of the slurry shows very similar fashion with the one without the catalyst indicating the inactivity of $Li_2MnP_2O_7$. The very small current (~50μA) at the applied the potential of 4.55 V vs Li/Li^+ scale is due to the capacitive charge

storage of carbon. In this regard, from the viewpoint of Li-ion battery cathode material, $Li_2MnP_2O_7$ is very inactive material because delithiation does not occur well at the room temperature as noted above. However, this inactiveness ensures us that Li ion does not leach during the OER.

The phase stability of the catalysts during the OER was observed by HRTEM and XRD analysis. HRTEM images revealed high crystallinity of the cycled samples both at the surface and the bulk. The fast Fourier transforms (FFTs) of the HRTEM images can be indexed with the crystal structure of $Li_{2-x}MnP_2O_7$ (Figure 3.14a, b) (see Figure 3.15 for $Li_{1.7}MnP_2O_7$ and $Li_{1.5}MnP_2O_7$). XRD analysis also indicates that the phase remained even after 100 cycles, without the appearance of any other phases or any broadening of the peaks (Figure 3.14c, d).

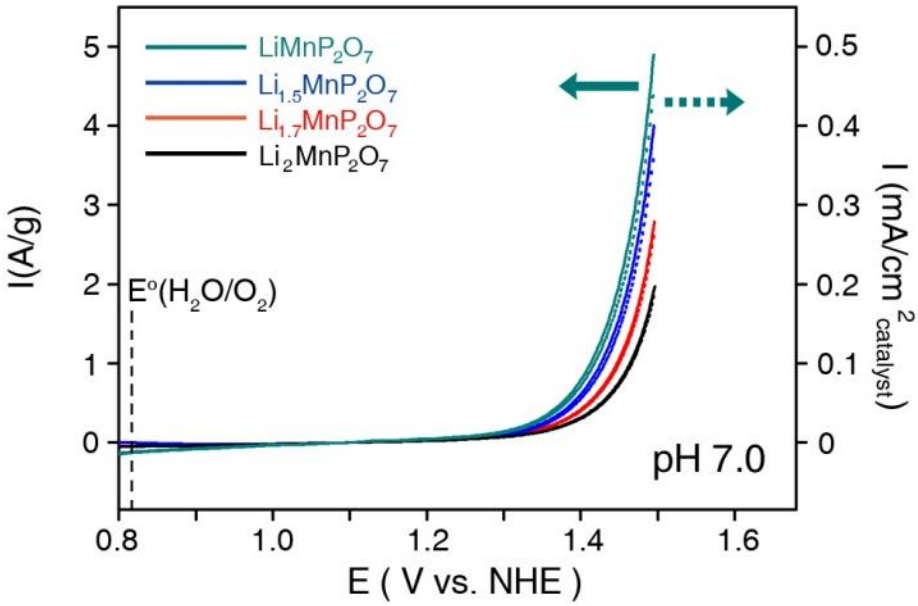

Figure 3. 4 Polarization-corrected cyclic voltammetry curves of $LiMnP_2O_7$ (green), $Li_{1.5}MnP_2O_7$ (blue), $Li_{1.7}MnP_2O_7$ (red) and $Li_2MnP_2O_7$ (black) in 0.5 M sodium phosphate buffer (pH 7.0). The polarization-corrected curves were obtained by averaging the currents of the forward and reverse CV scans. The current value was normalized by the total weight (solid line) and the total surface area of the catalyst (dashed line), respectively. The thermodynamic potential for water oxidation was plotted on the x-axis.

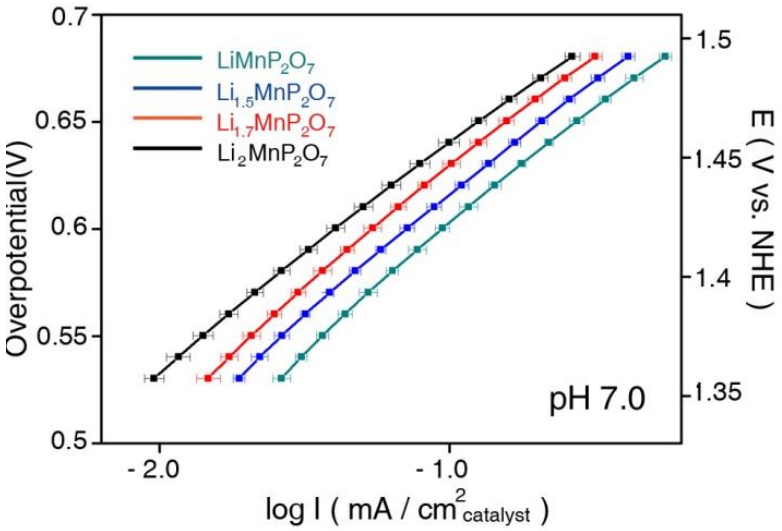

Figure 3. 5 Tafel plots for $LiMnP_2O_7$ (green), $Li_{1.5}MnP_2O_7$ (blue), $Li_{1.7}MnP_2O_7$ (red), $Li_2MnP_2O_7$ (black) where the current value was normalized by the total surface area of the compounds. The steady-state currents were averaged and the variations in the currents were indicated with error bars (n = 10).

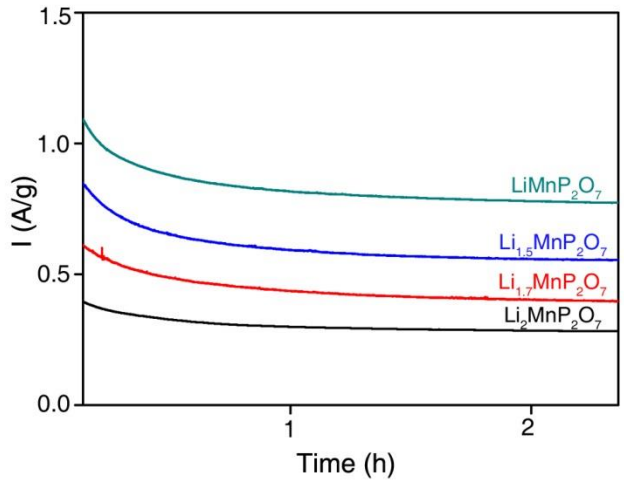

Figure 3. 6 Catalytic current profile of $Li_{2-x}MnP_2O_7$ (x = 0, 0.3, 0.5, 1) obtained under constant potential (1.4 V vs. NHE) electrolysis at pH 7.0. The saturated value is almost same with the averaged current shown in Figures 3a

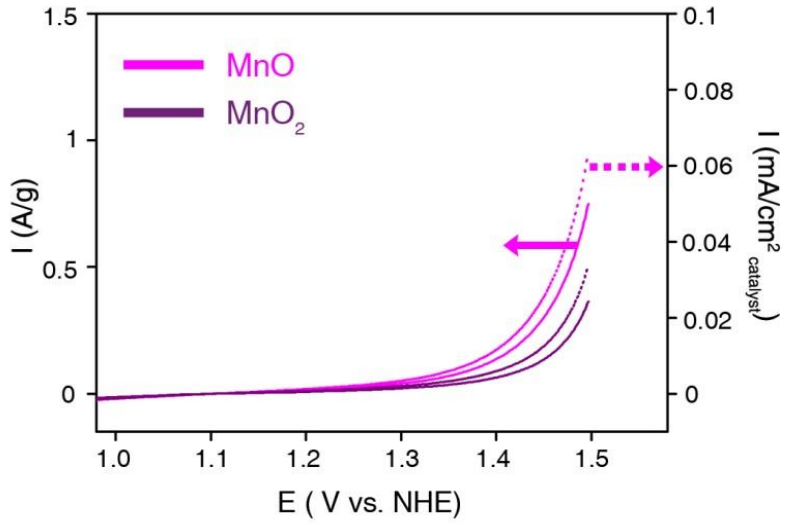

Figure 3. 7 Polarization-corrected cyclic voltammetry curves for MnO, MnO_2. The polarization-corrected curves were obtained by averaging the currents of the forward and reverse CV scans. The current value was normalized to the total weight (solid line) and the total surface area of the catalyst (dashed line), respectively. To obtain the Tafel plot, all the samples were normalized to the initial surface area of the particles on the working electrode. Particle surface area was obtained by BET analysis. (MnO : 1.18 m^2/g , MnO_2 : 1.08 m^2/g).

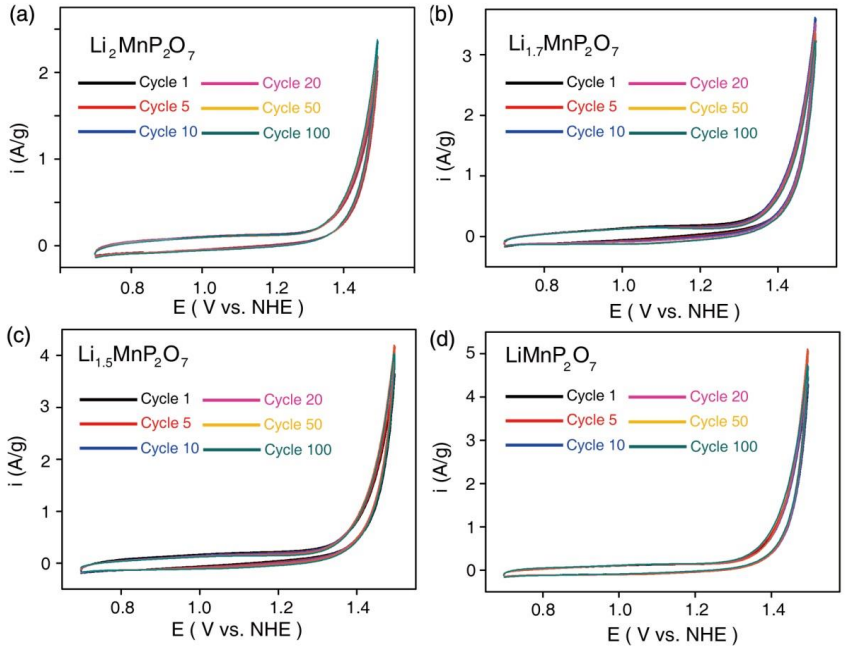

Figure 3. 8 Cyclic voltammetry curves of $Li_2MnP_2O_7$ (a), $Li_{1.7}MnP_2O_7$ (b), $Li_{1.5}MnP_2O_7$ (c) and $LiMnP_2O_7$ (d) before polarization correction. All the cyclic voltammetry curves were obtained in N_2-saturated 0.5 M sodium phosphate buffer (pH 7.0) at a scan rate of 10 mV/sec. Even after 100 cycles of voltammetry cycling, the OER currents and pseudocapacitive currents almost remained constant.

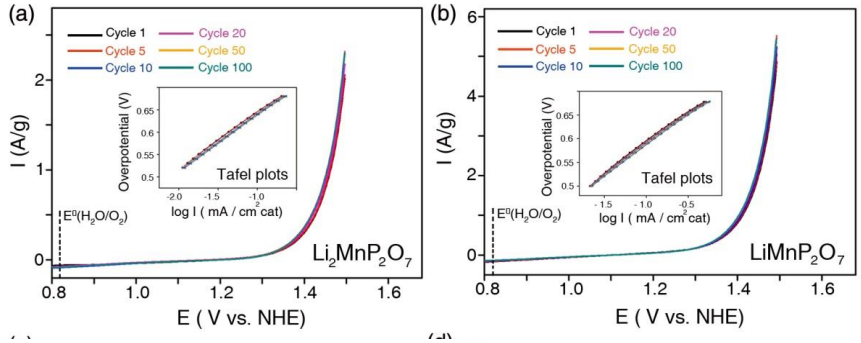

Figure 3. 9 Polarization-corrected cyclic voltammetry curves of $Li_2MnP_2O_7$ (a) and $LiMnP_2O_7$ (b) and their Tafel plots normalized to the surface area of the catalyst (inset) during 100 times of voltammetry cycling. The thermodynamic potential for water oxidation was plotted on the x-axis.

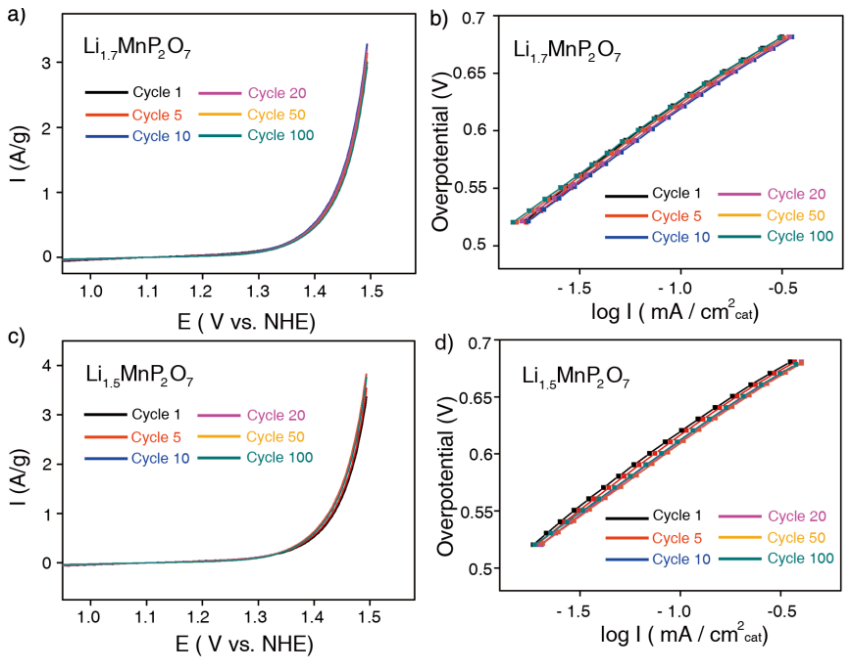

Figure 3. 10 Polarization-corrected cyclic voltammetry curves of $Li_{1.7}MnP_2O_7$ (a) and $Li_{1.5}MnP_2O_7$ (c) showing the 1st, 5th, 10th, 20th 50th, and 100th cycles. The polarization-corrected curves were obtained by averaging the currents of the forward and reverse CV scans. All the cyclic voltammetry curves were obtained in an N_2-saturated 0.5 M sodium phosphate buffer (pH 7.0) at a scan rate of 10 mV/sec. Tafel plots of the cycled data for selected cycles of $Li_{1.7}MnP_2O_7$ (b) and $Li_{1.5}MnP_2O_7$ (d).

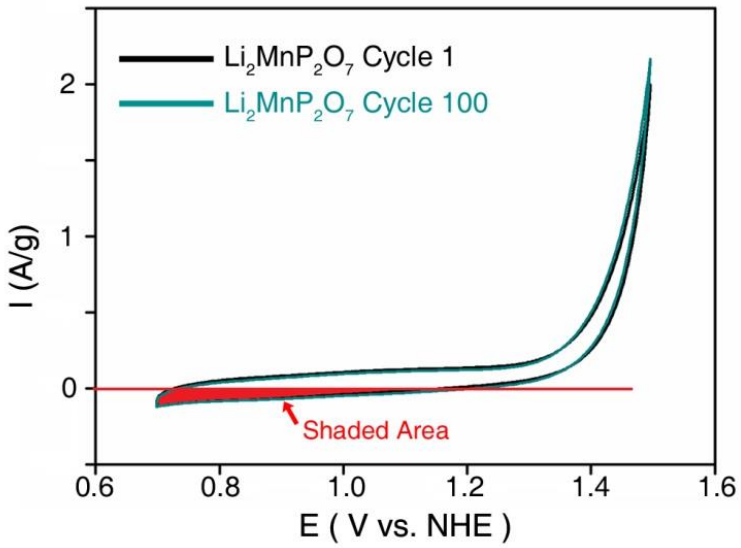

Figure 3. 11 Cyclic voltammetry curves of $Li_2MnP_2O_7$ showing 1st and 100th cycles where current was normalized to the weight of the it onto the FTO substrate. The shaded area during the negative-going scan can be proportional to the cathodic charge. The cathodic charge is proportional to the pseudocapacitance and the surface area of the catalysts onto the FTO substrate. The shaded areas of two curves were almost identical indicating surface area of the $Li_2MnP_2O_7$ maintains nearly constant during the OER.

Li/Mn ratio	Raw Sample	Bulk electrolyzed Sample (1.5 V vs NHE for 3hrs)
$Li_2MnP_2O_7$	2.017	1.991
$Li_{1.7}MnP_2O_7$	1.686	1.704
$Li_{1.5}MnP_2O_7$	1.523	1.546
$LiMnP_2O_7$	1.002	0.996

Table 3. 1 Inductively Coupled Plasma - Mass Spectrometer (ICP/MS) data for the $Li_{2-x}MnP_2O_7$ (x = 0, 0.3, 0.5, 1) powders before and after bulk-electrolysis at the potential of 1.5 V vs NHE for 3 hrs. After the OER, the ratio of the Li ions to Mn ions was maintained in each sample.

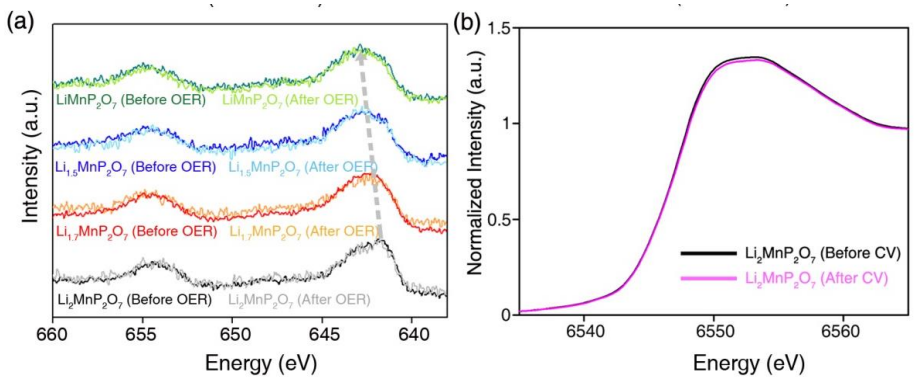

Figure 3. 12 (a) XPS spectra of the Mn 2p region of as-prepared and bulk-electrolyzed $Li_{2-x}MnP_2O_7$ (x = 0, 0.3, 0.5, 1) at the applied potential of 1.5 V vs NHE for 3hr. Mn $2p_{3/2}$ peak of bulk electrolyzed $Li_2MnP_2O_7$ (gray), $Li_{1.7}MnP_2O_7$ (orange), $Li_{1.5}MnP_2O_7$ (cyan), and $LiMnP_2O_7$ (green) at the surface shows similar value with that of as-prepared samples ($Li_2MnP_2O_7$ (black), $Li_{1.7}MnP_2O_7$ (red), $Li_{1.5}MnP_2O_7$ (blue), and $LiMnP_2O_7$ (olive)). (b)Ex-situ XANES spectra corresponding to Mn K-edge of the $Li_2MnP_2O_7$ before and after bulk-electrolysis at the applied potential of 1.5 V vs NHE for 3 hrs. All the electrochemical reaction was performed in 0.5 M sodium phosphate buffer at pH 7.0.

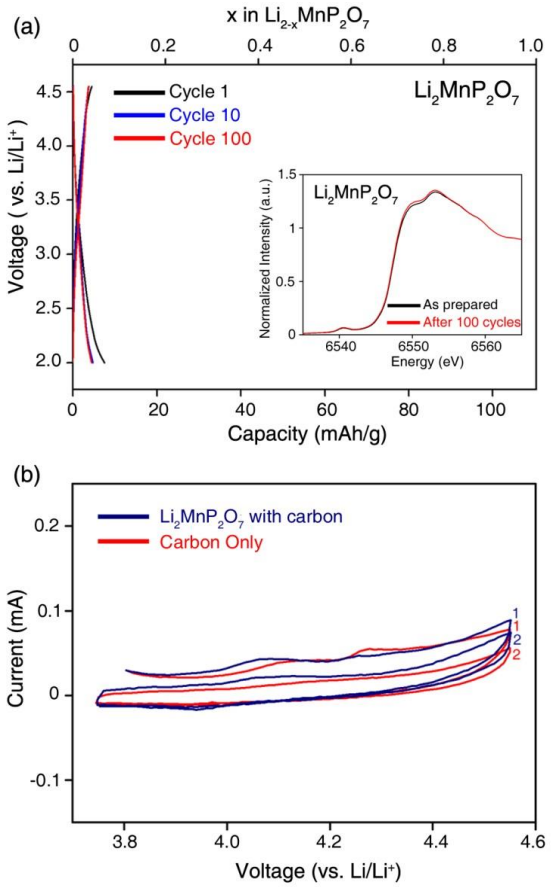

Figure 3.6 Electrochemical characterization of $Li_2MnP_2O_7$. (a) Galvanostatic voltage-composition curve of $Li_2MnP_2O_7$ at selected cycles (1st (black), 10th (blue), and 100th (red)) at a rate of C/20 obtained at 25δshowing very low capacity and no voltage plateau during charging and discharging. Inset shows the oxidation state of Mn was not changed after 100 cycles of charging and discharging using *ex-situ* XANES. (b) Cyclic voltammetry (CV) of $L_{i2}MnP_2O_7$ paste (blue) and carbon (red) conducted at 10 mV/s at 25℃.

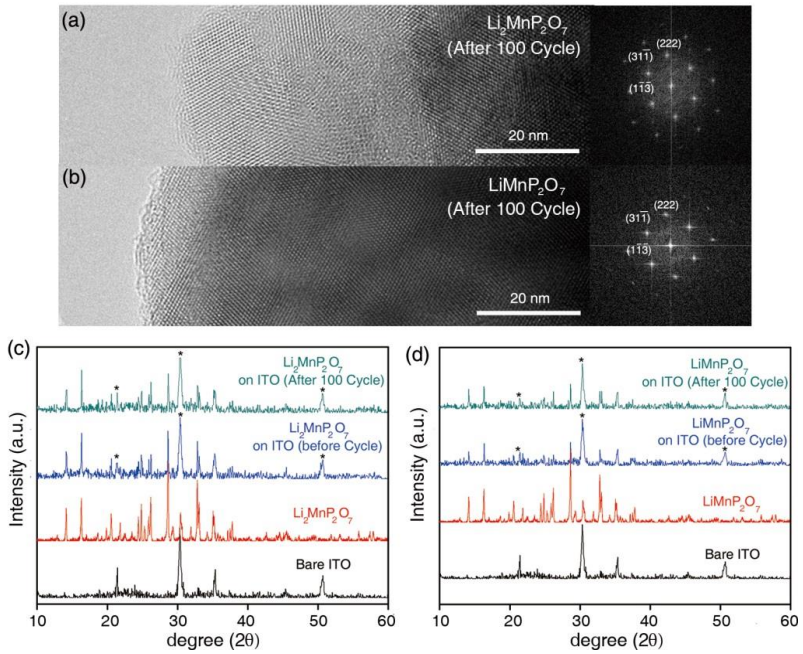

Figure 3. 7 HRTEM images (left) and FFTs (right) of the surface regions of $Li_2MnP_2O_7$ (a) and $LiMnP_2O_7$ (b) after 100 continuous cycles at a scan rate of 10 mV/s from 0.7 V to 1.5 V vs. NHE in a 0.5 M sodium phosphate buffer at pH 7.0. $Li_2MnP_2O_7$ (c) and $LiMnP_2O_7$ (d) films on an ITO (indium tin oxide) substrate before and after cycling 100 times from 0.7 V to 1.5 V vs. NHE at 10 mV/s in 0.5 M sodium phosphate buffer at pH 7.0. Asterisk (*) indicates peaks originating from ITO substrate. All the electrochemical reaction was performed in 0.5 M sodium phosphate buffer at pH 7.0.

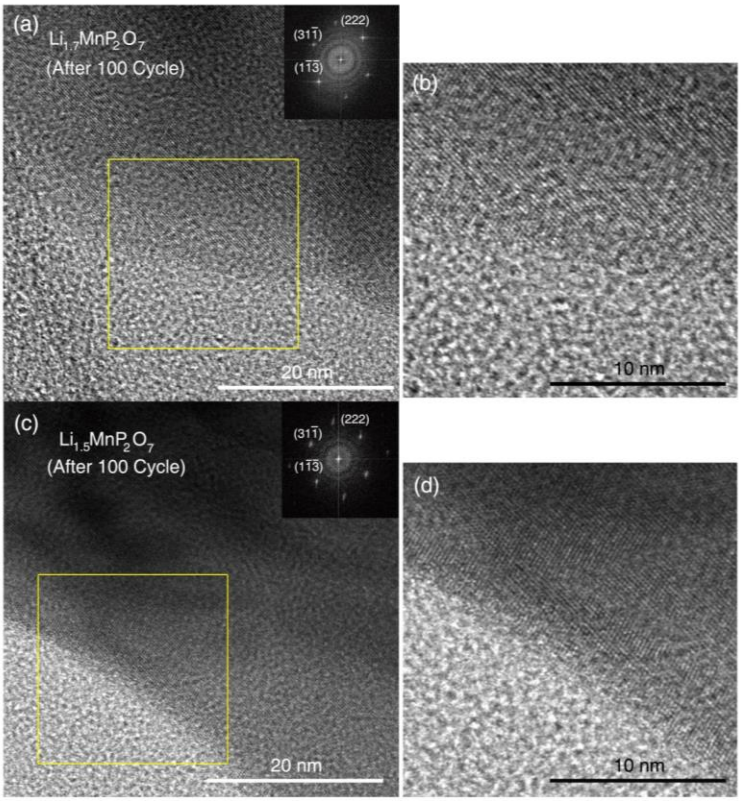

Figure 3. 8 HRTEM images (left) and FFTs (inset) of the interface regions of $Li_{1.7}MnP_2O_7$ (a) and $Li_{1.5}MnP_2O_7$ (c) after 100 continuous cycles at a scan rate of 10 mV/s from 0.7 V to 1.5 V vs. NHE in 0.5 M sodium phosphate buffer at pH 7. (b) and (d) are high magnitude images of selected areas (yellow squares) of (a) and (b), respectively. HRTEM images for $Li_{1.7}MnP_2O_7$ and $Li_{1.5}MnP_2O_7$ also revealed high crystallinity even after 100 cycles from 0.7 V to 1.5 V versus NHE.

3.2.3 Mechanistic studies of $Li_{2-x}MnP_2O_7$ (x=0~1)

The valency state and local environments of Mn in the atomistic level was investigated by performing DFT calculations. A series of possible crystal structures of $Li_{2-x}MnP_2O_7$ (x = 0.25, 0.5, 1) and their relative energies were identified which supported its monophasic reaction at room temperature (Figure 3.16) We selected the most stable structures in each composition (x = 0.25, 0.5, 1) as the theoretical models of $Li_{1.75}MnP_2O_7$, $Li_{1.5}MnP_2O_7$, and $LiMnP_2O_7$ structures (Figure 3.17). The charges of Mn in $Li_{2-x}MnP_2O_7$, which were determined using the Voronoi spin integration, was consistent with the XPS results. The average oxidation state of Mn atom gradually changed upon delithiation from 2 to 3. We found that the charges are delocalized among both 5-coordinated and 6-coordinated Mn sites in $Li_{1.75}MnP_2O_7$ (Figure 3.17b). However, charge localization was observed in $Li_{1.5}MnP_2O_7$, where two of the TBP sites are Mn(III), while only one of the two Oh sites is Mn(III) (Figure 3.17c). Finally, all of the Mn(II) atoms undergo oxidation to Mn(III) when full delithiation occurs for $Li_2MnP_2O_7$ ($LiMnP_2O_7$) (Figure 3.17d). Interestingly, in $LiMnP_2O_7$, all the Oh Mn sites transform into TBP by breaking the edge sharing Mn-O bonds in the Mn_2O_9 subunit (Figure 3.17d). As a result, delithiation allows all of the Mn ions to be positioned in 5-coordinate sites.

From the calculated lattice parameters and the unit cell volume of $Li_{2-x}MnP_2O_7$ (x = 0, 0.25, 0.5, 1), we could confirm that the changes in the

lattice parameters and unit cell volume were very small; this finding was consistent with experimentally obtained results from XRD analysis (Table 3.2). This small change in lattice parameter supports our idea that $Li_{2-x}MnP_2O_7$ can be a good platform for understanding the role of Mn valency in water catalysis with minimal change in structural factors. Moreover, there is negligible volume change, ~ 1 %, between $LiMnP_2O_7$ and $Li_2MnP_2O_7$. Note that the unit cell volume normalized to the number of total Mn atoms in the unit cell of Mn(II)O is 87.8 $Å^3$/Mn, which is 18.8 % smaller than that of $Mn(III)_2O_3$ (104.3 $Å^3$/Mn). HRTEM analysis of our catalysts shows that the local structure of the surface resembles with that of the bulk. Therefore, atomic structure of the bulk material could be a good platform to make a discussion how Mn valency affects the catalytic effect. Indeed, based on HRTEM analysis, previous reports selected the atomic structure of each bulk material as a starting point to find the correlations between the crystal structure of the catalysts and their catalytic rate.[70] Although resting state of Mn atoms during the OER is important for understanding the true activity of the catalysts, initial oxidation state of Mn atoms also affects the initial Mn local environment and the catalytic activity.[70] Indeed, many previous works explained the activity of the catalysts based on their initial local structure. Therefore, in order to find the general relationship between the catalytic rate and the atomic structure of our catalysts, we firstly focused on the local Mn atomic structure of bulk structures of calculated $Li_{2-x}MnP_2O_7$ (x = 0, 0.25, 0.5,

1).

The Mn-Mn and Mn-O bond distances for $Li_{2-x}MnP_2O_7$ (x = 0, 0.25, 0.5, 1) was calculated from their theoretical structures. Notably, the average di- μ -oxo Mn-Mn distances and the second Mn-Mn distances were approximately the same among samples of $Li_2MnP_2O_7$, $Li_{1.75}MnP_2O_7$, and $Li_{1.5}MnP_2O_7$. Here, the inter-manganese distance, where two Mn atoms are most closely connected by one P_2O_7 group, is notated as second Mn-Mn distance. For example, the second Mn-Mn distance of $Li_{1.5}MnP_2O_7$ was 5.051 Å, which is only 0.041 Å larger than that of $Li_2MnP_2O_7$ (5.010 Å) (Table 3.3). The average Mn-O distance of $Li_{2-x}MnP_2O_7$ gradually decreases from 2.183 Å to 2.033 Å as delithiation proceeds. It is attributed to the oxidation of Mn ions to a higher value with shorter Mn-O bonds.

According to previous studies,[71] the bond distances of Mn-Mn and Mn-O are good indicators for the prediction of catalytic properties. It has been generalized that longer Mn-Mn and Mn-O distances are favorable for OER catalysis. The Dismukes group reported that longer and weaker Mn-Mn and Mn-O bond-containing catalysts tend to exhibit better performance. [70] The Dau group also reported that amorphous MnO_x, which has longer Mn-Mn distances, exhibits higher catalytic performance.[53] In our case, we observed that the compound with larger Mn-Mn distance in bulk structures shows higher catalytic ability which generally agrees with previous works.[71] However, it was noted that changes in the Mn-Mn distance are significantly

smaller when considering the large catalytic enhancement. From $Li_2MnP_2O_7$ to $Li_{1.75}MnP_2O_7$ and from $Li_{1.75}MnP_2O_7$ to $Li_{1.5}MnP_2O_7$, the increasing ratios of the average di- μ -oxo Mn-Mn distance were only 1.2 % and 0.84 %, respectively. These values represent small changes compared to the changes in Mn-Mn distances in conventional Mn-oxide compounds. From Mn(II)O to $Mn(III)_2O_3$, the second Mn-Mn distance and the average di- μ -oxo distance increased by 25 % and 1.8 %, respectively. Here, the second Mn-Mn distances in MnO and Mn_2O_3 refer to the average mono- μ -oxo Mn-Mn distance. Furthermore, the largest change in the Mn-Mn distance was 6.0 %, resulting from $Li_{1.5}MnP_2O_7$ to $LiMnP_2O_7$; however, that change does not lead to a greater enhancement of OER during this step. If the Mn-Mn bond distance determines the catalytic activity, the difference between the current density of $Li_{1.5}MnP_2O_7$ and $LiMnP_2O_7$ should be much larger than that between the current density of $Li_{1.75}MnP_2O_7$ and $Li_{1.5}MnP_2O_7$ or $Li_2MnP_2O_7$ and $Li_{1.75}MnP_2O_7$. However, the current density is gradually enhanced as lithium contents decreased (Figure 3.4). We believe that although the effect of the Mn-Mn distance change cannot be completely excluded, it is fair to mention that the Mn-Mn distance change in $Li_{2-x}MnP_2O_7$ remains only a marginal role in the catalytic enhancement.

Previous studies concerning various Mn-containing catalysts have suggested that catalysts with weaker and longer Mn-O bonds exhibited higher OER activity than those with stronger and shorter Mn-O bonds. However, this conclusion contrasts with our results, which show that the Mn-O distance in

bulk structures decreased from 2.183 Å in low-catalytic $Li_2MnP_2O_7$ to 2.033 Å in high-catalytic $LiMnP_2O_7$. If the Mn-O bond is the dominant factor in OER activity, the reduction of the Mn-O bond from $Li_2MnP_2O_7$ to $LiMnP_2O_7$ in the same crystal frameworks should lead to inferior catalytic activity. In this regard, we can conceive that the effect of valency dominates over structural factors, such as Mn-O or Mn-Mn bond distances in the crystal.

Moreover, in order to further understand the catalysts' surface structure where OER occurs, we performed additional DFT calculations from GGA+U. The local Mn atom environment at the most stable surface of each catalyst were found with the well-established surface cleaving method.[90] In order to depict the atomic structure of the surface, the atoms near 10 Å range from surface were fully relaxed and vaccum slab of 15 Å were used. Furthermore, water molecules were introduced to the surface to simulate the initial situation of the electrolysis near Mn atoms. Note that for the surface of $Li_2MnP_2O_7$ and $LiMnP_2O_7$, there are empty sites where water can be adsorbed. The most stable positions of water molecules at the surface were determined by relaxing the overall structure. The local Mn environment and the water molecules at the surface of $Li_2MnP_2O_7$ and $LiMnP_2O_7$ were shown in Figure 3.18. All the Mn atoms at the surface of $Li_2MnP_2O_7$ and $LiMnP_2O_7$ have 5-coordination when Mn-H_2O bonds form.

Based on the calculated surface structures of $Li_2MnP_2O_7$ and $LiMnP_2O_7$, we compared the averaged Mn-O distance and di- μ -oxo Mn-Mn

distance around the Mn atoms at the surface (Table 3.3). The averaged Mn-O distance decreased from 2.173 Å in $Li_2MnP_2O_7$ to 2.008 Å in $LiMnP_2O_7$. Interestingly, the di- μ -oxo Mn-Mn distance decreased from 3.313 Å in $Li_2MnP_2O_7$ to 3.193 Å in $LiMnP_2O_7$. This trend is opposite to that observed in bulk structures of $Li_{2-x}MnP_2O_7$. However, the decreased di- μ -oxo Mn-Mn distance and averaged Mn-O distance at the surface Mn atoms along the delithiation further supports our claim that the Mn-Mn and Mn-O distance change in $Li_{2-x}MnP_2O_7$ might play a marginal role in the enhancement of the catalytic ability.

We believe that the gradually changed Mn valency and occupancy of the d states upon delithiation has affected the catalytic activities of $Li_{2-x}MnP_2O_7$. Previous works indicated that the relationship between e_g occupancy in a transition metal and the 2p level of oxygen-related species (*OH, *O, *OOH) is a crucial factor for the OER activity of a transition-metal based catalyst.[91-92] Recently, Dismukes group revealed that Mn based oxides with e_g^1 orbital generally shows high catalytic activity.[70] Moreover, Rao group emphasized the role of e_g^1 configuration on water oxidation catalysis using Co^{3+} (t_{2g}^5 e_g^1) and Mn^{3+} (t_{2g}^3 e_g^1) based oxide materials.[93] The change of the Mn valency in the series of $Li_{2-x}MnP_2O_7$ was able to nicely tune the occupation of d states from e_g^2 to e_g^1, and might result in a higher catalysis of water oxidation.

We investigated another possible role of Mn valency from the

viewpoint of the asymmetric local Mn environment. Previous studies quantified the degree of Mn polyhedron distortion (△) also known as the Baur distortion index, using the following formula [94]:

$$\Delta = \frac{1}{N}\sum_{k=1}^{N}\frac{|\ d_k - d_m\ |}{d_m}$$

where d_k and d_m are individual Mn-O bond lengths and mean values, respectively, and N is the number of Mn-O bonds in one polyhedron. The distortion indices of Mn polyhedra in $Li_{2-x}MnP_2O_7$ are summarized in Table 3.4. As the lithium content decreases in $Li_{2-x}MnP_2O_7$, the average distortion index of the Mn polyhedron increases from 0.0191 in $Li_2MnP_2O_7$ to 0.0540 in $LiMnP_2O_7$. This effect occurs because Mn(III) induces Jahn-Teller distortion, which asymmetrically elongates some Mn-O bonds while shortening others. To our surprise, we find that the linear increase in distortion exhibits a trend similar to that of the catalytic enhancement of $Li_{2-x}MnP_2O_7$, as shown in Figure 3.19. This linear relationship implies that the asymmetric Mn environments affect the catalytic ability of Mn-containing catalysts during water oxidation catalysis.

Moreover, we calculated the local distortion index of the Mn atoms at the surface of $Li_2MnP_2O_7$ and $LiMnP_2O_7$. The distortion index of the surface Mn atoms was calculated from the five-coordinated Mn atoms at the

surface where Mn-H_2O bonds form. Interestingly, the average local distortion index of Mn atoms at the surface of $LiMnP_2O_7$ (0.0557) shows higher value than that at the surface of $Li_2MnP_2O_7$ (0.0294). Although the distortion index values at the surface and the bulk of each catalyst are slightly different, the general trend that distortion index increases after delithiation is still observed for the surface of the catalysts. While the distortion indexes of $Li_{1.75}MnP_2O_7$ and $Li_{1.5}MnP_2O_7$ are still under investigation due to the complexities in determining the surface of off stoichiometric compounds. However, based on the both end cases of $Li_2MnP_2O_7$ surface and $LiMnP_2O_7$ surface, we can propose that the distortion index can be another good descriptor for predicting the catalytic ability of Mn compounds.

We speculate that the distorted Mn geometry in $Li_2MnP_2O_7$ could contribute to the stabilization of Mn(III) under neutral conditions. It is well known that the symmetric MnO_6 octahedron in MnO and MnO_2 becomes unstable when Mn(III) is generated during the catalysis; consequently, Mn(III) rapidly dissociates into Mn(II) and Mn(IV) via a charge disproportionation (CD) process under neutral conditions.[57] Thus, an intrinsically distorted crystal structure is favorable for stabilizing the Mn(III) state because the CD process can be suppressed in this structure.[57,70] Indeed, it has been reported that the asymmetric Mn orbital in partially N-doped δ-MnO_2 could stabilize the Mn(III) state under neutral conditions by inhibiting the CD process, and consequently exhibit excellent OER catalytic behavior.[60] It is noteworthy that

the distortion index value of $Li_2MnP_2O_7$ is 0.0191 while that of MnO or δ-MnO_2 is 0. Additionally, we think that the TBP polyhedron in $Li_2MnP_2O_7$ can further stabilize Mn(III) during the catalytic cycle. The TBP polyhedron can be regarded as a highly distorted Oh polyhedron where one Mn-O bond length is exceptionally large tomaintain its bond. Because the five-coordinate MnO_5 is not subject to Jahn-Teller effect,[95] the exchange of Mn valency during catalysis requires relatively small local change, stabilizing the structure against the CD process..

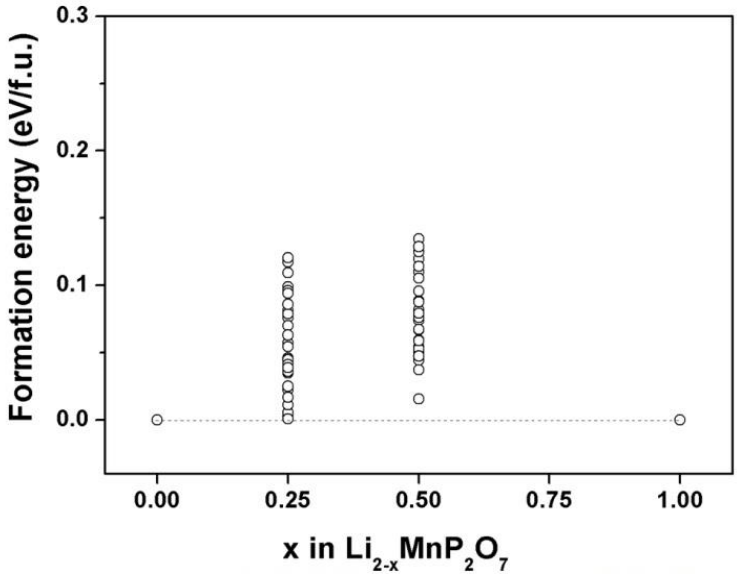

Figure 3. 9 Calculated formation energies at various compositions (x= 0, 0.25, 0.5, 1) and a convex hull of $Li_{2-x}MnP_2O_7$. A series of possible crystal structures of $Li_{2-x}MnP_2O_7$ (x = 0.25, 0.5, 1) and their relative energies were identified (blank circle). We selected the most stable structures in each composition (x = 0.25, 0.5, 1) as the theoretical models of $Li_{1.75}MnP_2O_7$, $Li_{1.5}MnP_2O_7$, and $LiMnP_2O_7$ structures.

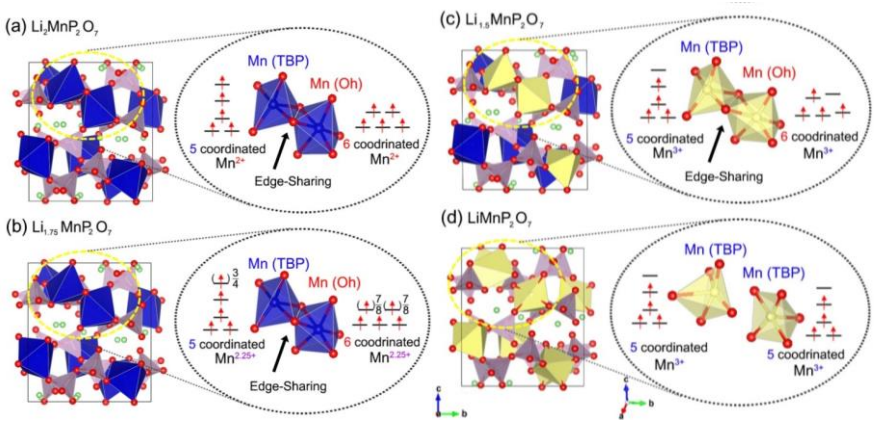

Figure 3. 10 Simulated crystal structures of the $Li_2MnP_2O_7$ (a), $Li_{1.75}MnP_2O_7$ (b), $Li_{1.5}MnP_2O_7$ (c), and $LiMnP_2O_7$ (d) unit cells. Inset shows the local Mn environment around the Mn_2O_9 subunit. Mn^{2+} atoms and Mn^{3+} atoms in the unit cell are shown in blue and yellow, respectively. In $Li_{1.75}MnP_2O_7$, charge delocalization occurs and all of the Mn atoms have an average oxidation state of 2.25. (↑) 3/4 and (↑)7/8, indicating that the electron occupancies in each of the orbitals are 3/4 and 7/8, respectively. (b). In $Li_{1.5}MnP_2O_7$, three Mn^{2+} atoms were oxidized into Mn^{3+}, and the remaining five Mn atoms have an average oxidation state of 2.2. (c) All Mn^{2+} is oxidized into Mn^{3+} and all of the Oh Mn sites transforms into TBP (d).

Designation	*a* (Å)	*b* (Å)	*c* (Å)	β(deg)	Vol ($Å^3$)
$Li_2MnP_2O_7$	9.916	9.829	11.180	102.467	1063.930
$Li_{1.75}MnP_2O_7$	9.909	9.894	11.282	102.283	1080.859
$Li_{1.5}MnP_2O_7$	9.916	9.850	11.223	101.833	1072.864
$LiMnP_2O_7$	9.978	9.666	11.085	99.868	1053.371

Table 3. 2 Simulated lattice parameters and unit cell volume of $Li_{2-x}MnP_2O_7$.

Designation	Avg. di-μ-oxo Mn-Mn distance (Bulk)	Second Mn-Mn distance (Bulk)	Avg. Mn-O distance (Bulk)
$Li_2MnP_2O_7$	3.302	5.010	2.183
$Li_{1.75}MnP_2O_7$	3.343	4.967	2.168
$Li_{1.5}MnP_2O_7$	3.371	5.051	2.144
$LiMnP_2O_7$	3.574	4.979	2.033
MnO	3.168	4.480	2.265
Mn_2O_3	3.111	3.578	2.060

Designation	Avg. di- μ -oxo Mn-Mn distance (Surface)	Avg. Mn-O distance (Surface)
$Li_2MnP_2O_7$	3.313	2.173
$LiMnP_2O_7$	3.193	2.008

Table 3. 3 Selected structural parameters of calculated $Li_{2-x}MnP_2O_7$ (x = 0, 0.25, 0.5, 1) , MnO, and Mn_2O_3.

	Mn(1)	Mn(2)	Avg.
$Li_2MnP_2O_7$ (Bulk)	0.0159	0.0222	0.0191
$Li_{1.7}MnP_2O_7$ (Bulk)	0.0240	0.0299	0.0270
$Li_{1.5}MnP_2O_7$ (Bulk)	0.0322	0.0440	0.0381
$LiMnP_2O_7$ (Bulk)	0.0822	0.0257	0.0540
$Li_2MnP_2O_7$ (Surface)	0.0322	0.0267	0.0294
$LiMnP_2O_7$ (Surface)	0.0603	0.0511	0.0557

Table 3. 4 Distortion index of calculated $Li_{2-x}MnP_2O_7$ (x = 0, 0.25, 0.5, 1).

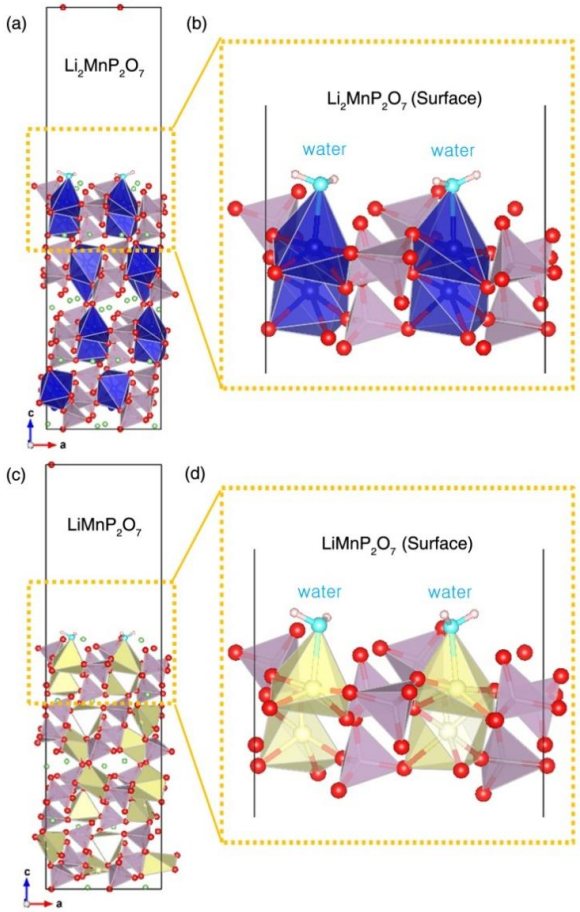

Figure 3. 11 The local environment of the Mn atoms at the surface of $Li_2MnP_2O_7$ (a) and $LiMnP_2O_7$ (c). Magnified images of (a) and (c) were shown in (b) and (d), respectively. Mn atoms at the surface in $Li_2MnP_2O_7$ and $LiMnP_2O_7$ have open coordination sites where water molecules bind which can be served as the substrate for the water oxidation. Mn(II) atoms Mn(III) atoms and water molecules are illustrated in blue, yellow and cyan, respectively.

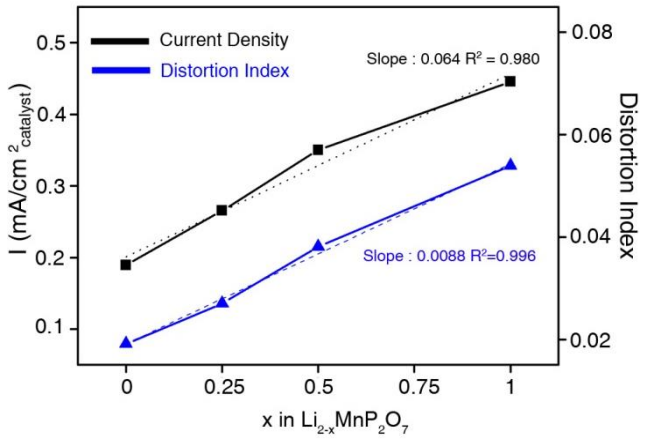

Figure 3. 12 The catalytic current density at the overpotential value of 680 mV (black) and the distortion index value (△) (blue) as a function of delithiated amount (x) in $Li_{2-x}MnP_2O_7$. The current density was normalized to the surface area of the catalysts and the distortion index value was calculated from the definition of the Baur distortion index. The linear trend of both the current density (dashed black line, slope: 0.064, R^2 = 0.980) and distortion index value (dashed blue line, slope: 0.0088, R^2 = 0.996) is clearly shown.

Chapter 4. Conclusion

In Chapter 2, we have presented a new crystalline phase, $Mn_3(PO_4)_2$-$3H_2O$, that acts as an efficient OER catalyst. We found that Mn atoms have an asymmetric geometry in the crystal and display a distorted crystal field with phosphate groups and water molecules. $Mn_3(PO_4)_2$-$3H_2O$ exhibits superior catalytic performance compared to MnO and MnO_2 catalysts under neutral pH. Moreover, EPR analysis revealed the formation of Mn^{III} during catalytic cycle. DFT theoretical calculations verified the experimental observation that Mn^{II} atoms can be easily oxidized into Mn^{III} species through J-T distortion which is stabilized by its structural nature, the distorted and flexible crystal field around the Mn atoms. We expect that the discovery of this new $Mn_3(PO_4)_2$-$3H_2O$ crystal and the relationship between its structural features and catalytic performance will provide insights useful for the development of divalent Mn-based catalysts.

In Chapter 3, our studies demonstrate the possibility of a new pyrophosphate-based Mn crystal, $Li_2MnP_2O_7$, as an efficient water oxidation catalyst under neutral conditions for the first time. By tuning the manganese valency in $Li_2MnP_2O_7$, we can observe the effect of the Mn(III) state itself on water oxidation catalysis with minimal crystallographic change. $Li_{2-x}MnP_2O_7$ compounds show catalytic stability up to 1.5 V vs NHE without additional

delithiation or phase transformation ensuring us for understanding the effect of oxidation state of manganese on water oxidation catalysis based on their catalytic activites. A higher Mn(III) content in the catalyst can boost catalytic activity by increasing the degree of distortion in local Mn environment both at the surface and the bulk $Li_{2-x}MnP_2O_7$. We expect that the results highlight the understanding of the effect of the Mn oxidation state on the oxygen evolution reaction and can provide valuable insight for developing a new Mn-based water oxidation catalyst. Moreover, our approach can be applied to construct the design rule for other transition metal (Co, Ni, Fe, Cu)-based water oxidation catalysts.

References

[1] Armaroli, N.; Balzani, V. *Angew. Chem. Int. Ed.* 2007, *46*, 52

[2] Simmons, M. R. *Twilight in the desert: The coming Saudi oil shock and the world economy*; Wiley.com, 2006.

[3] Power, F. *Science* 2006, *311*, 1380.

[4] Inman, M. *Science* 2005, 309, 1170.

[5] Ragauskas, A. J.; Williams, C. K.; Davison, B. H.; Britovsek, G.; Cairney, J.; Eckert, C. A.; Frederick, W. J.; Hallett, J. P.; Leak, D. J.; Liotta, C. L. *Science* 2006, *311*, 484.

[6] SERVICE, R. F. *Science(Washington, D. C.)* 2005, *309*, 548

[7] Walter, M. G.; Warren, E. L.; McKone, J. R.; Boettcher, S. W.; Mi, Q.; Santori, E. A.; Lewis, N. S. *Chem. Rev.* 2010, *110*, 6446

[8] Lewis, N. S.; Nocera, D. G. *Proc. Natl. Acad. Sci. U.S.A.* 2006, *103*, 15729.

[9] Bard, A. J.; Fox, M. A. *Acc. Chem. Res.* 1995, *28*, 141.

[10] Gust, D.; Moore, T. A.; Moore, A. L. *Acc. Chem. Res.* 2009, *42*, 1890.

[11] Swierk, J. R.; Mallouk, T. E. *Chem. Soc. Rev.* 2013, *42*, 2357.

[12] Grätzel, M. *Nature* 2001, 414, 338

[13] Meyer, T. J. *Acc. Chem. Res.* 1989, *22*, 163.

[14] Barber, J. *Chem. Soc. Rev.* 2009, *38*, 185.

[15] Faunce, T. A.; Lubitz, W.; Rutherford, A. W.; MacFarlane, D.; Moore, G.

F.; Yang, P.; Nocera, D. G.; Moore, T. A.; Gregory, D. H.; Fukuzumi, S.; Yoon, K. B.; Armstrong, F. A.; Wasielewski, M. R.; Styring, S. *Energy Environ. Sci.* 2013, *6*, 695.

[16] Loll, B.; Kern, J.; Saenger, W.; Zouni, A.; Biesiadka, J. *Nature* 2005, *438*, 1040.

[17] Yano, J.; Kern, J.; Sauer, K.; Latimer, M. J.; Pushkar, Y.; Biesiadka, J.; Loll, B.; Saenger, W.; Messinger, J.; Zouni, A.; Yachandra, V. K. *Science* 2006, *314*, 821.

[18] Ferreira, K. N.; Iverson, T. M.; Maghlaoui, K.; Barber, J.; Iwata, S. *Science* 2004, *303*, 1831.

[19] Umena, Y.; Kawakami, K.; Shen, J.-R.; Kamiya, N. *Nature* 2011, *473*, 55.

[20] Roelofs, T. A.; Liang, W.; Latimer, M. J.; Cinco, R. M.; Rompel, A.; Andrews, J. C.; Sauer, K.; Yachandra, V. K.; Klein, M. P. *Proc. Natl. Acad. Sci. U.S.A.* 1996, *93*, 3335.

[21] Dau, H.; Iuzzolino, L.; Dittmer, J. *BBA. Bioenergetics* 2001, *1503*, 24.

[22] Kanan, M. W.; Nocera, D. G. *Science* 2008, *321*, 1072.

[23] Betley, T. A.; Wu, Q.; Van Voorhis, T.; Nocera, D. G. *Inorg. Chem.* 2008, *47*, 1849.

[24] Fujishima, A. *Nature* 1972, *238*, 37

[25] Man, I. C.; Su, H. Y.; Calle-Vallejo, F.; Hansen, H. A.; Martínez, J. I.; Inoglu, N. G.; Kitchin, J.; Jaramillo, T. F.; Nørskov, J. K.; Rossmeisl, J.

ChemCatChem 2011, *3*, 1159

[26] Rasiyah, P.; Tseung, A. *J. Electrochem. Soc.* 1984, *131*, 803.

[27] Trasatti, S. *Electrochim. Acta*. 1984, *29*, 1503.

[28] Bockris, J. O.; Otagawa, T. *J. Phys. Chem.* 1983, *87*, 2960

[29] Suntivich, J.; May, K. J.; Gasteiger, H. A.; Goodenough, J. B.; Shao-Horn, Y. *Science* 2011, *334*, 1383

[30] Smith, R. D.; Prévot, M. S.; Fagan, R. D.; Zhang, Z.; Sedach, P. A.; Siu, M. K. J.; Trudel, S.; Berlinguette, C. P. *Science* 2013, *340*, 60

[31] Youngblood, W. J.; Lee, S.-H. A.; Kobayashi, Y.; Hernandez-Pagan, E. A.; Hoertz, P. G.; Moore, T. A.; Moore, A. L.; Gust, D.; Mallouk, T. E. *J. Am. Chem. Soc.* 2009, *131*, 926.

[32] Liu, F.; Concepcion, J. J.; Jurss, J. W.; Cardolaccia, T.; Templeton, J. L.; Meyer, T. J. *Inorg. Chem.* 2008, *47*, 1727.

[33] Duan, L.; Bozoglian, F.; Mandal, S.; Stewart, B.; Privalov, T.; Llobet, A.; Sun, L. *Nat. Chem.* 2012, *4*, 418.

[34] Zhao, Y.; Swierk, J. R.; Megiatto, J. D.; Sherman, B.; Youngblood, W. J.; Qin, D.; Lentz, D. M.; Moore, A. L.; Moore, T. A.; Gust, D.; Mallouk, T. E. *Proc. Natl. Acad. Sci. U.S.A.* 2012, *109*, 15612.

[35] Kanan, M. W.; Yano, J.; Surendranath, Y.; Dincă, M.; Yachandra, V. K.; Nocera, D. G. *J. Am. Chem. Soc.* 2010, *132*, 13692.

[36] Dincă, M.; Surendranath, Y.; Nocera, D. G. *Proc. Natl. Acad. Sci. U.S.A.* 2010, *107*, 10337

[37] Gong, M.; Li, Y.; Wang, H.; Liang, Y.; Wu, J. Z.; Zhou, J.; Wang, J.; Regier, T.; Wei, F.; Dai, H. *J. Am. Chem. Soc.* 2013

[38] McCrory, C. C.; Jung, S.; Peters, J. C.; Jaramillo, T. F. *J. Am. Chem. Soc.* 2013

[39] Yagi, M.; Kaneko, M. *Chem. Rev.* 2001, *101*, 21

[40] Zhang, M.-T.; Chen, Z.; Kang, P.; Meyer, T. J. *J. Am. Chem. Soc.* 2013, *135*, 2048

[41] Zhong, D. K.; Cornuz, M.; Sivula, K.; Grätzel, M.; Gamelin, D. R. *Energy Environ. Sci.* 2011, *4*, 1759

[42] Zhong, D. K.; Choi, S.; Gamelin, D. R. *J. Am. Chem. Soc.* 2011, *133*, 18370

[43] Du, C.; Yang, X.; Mayer, M. T.; Hoyt, H.; Xie, J.; McMahon, G.; Bischoping, G.; Wang, D. *Angew. Chem. Int. Ed.* 2013, *52*, 12692

[44] Ruettinger, W. F.; Ho, D. M.; Dismukes, G. C. *Inorg. Chem.* 1999, *38*, 1036.

[45] Hocking, R. K.; Brimblecombe, R.; Chang, L.-Y.; Singh, A.; Cheah, M. H.; Glover, C.; Casey, W. H.; Spiccia, L. *Nat. Chem.* 2011, *3*, 461.

[46] Kanady, J. S.; Tsui, E. Y.; Day, M. W.; Agapie, T. *Science* 2011, *333*, 733.

[47] Tsui, E. Y.; Tran, R.; Yano, J.; Agapie, T. *Nat. Chem.* 2013

[48] Najafpour, M. M.; Ehrenberg, T.; Wiechen, M.; Kurz, P. *Angew. Chem. Int. Ed.* 2010, *49*, 2233.

[49] Brimblecombe, R.; Kolling, D. R. J.; Bond, A. M.; Dismukes, G. C.;

Swiegers, G. F.; Spiccia, L. *Inorg. Chem.* 2009, *48*, 7269.

[50] Fekete, M.; Hocking, R. K.; Chang, S. L. Y.; Italiano, C.; Patti, A. F.; Arena, F.; Spiccia, L. *Energy Environ. Sci.* 2013, *6*, 2222.

[51] Jiao, F.; Frei, H. *Chem. Comm.* 2010, *46*, 2920.

[52] Gorlin, Y.; Jaramillo, T. F. *J. Am. Chem. Soc.* 2010, *132*, 13612.

[53] Zaharieva, I.; Chernev, P.; Risch, M.; Klingan, K.; Kohlhoff, M.; Fischer, A.; Dau, H. *Energy Environ. Sci.* 2012, *5*, 708.

[54] Robinson, D. M.; Go, Y. B.; Greenblatt, M.; Dismukes, G. C. *J. Am. Chem. Soc.* 2010, *132*, 11467.

[55] Indra, A.; Menezes, P. W.; Zaharieva, I.; Baktash, E.; Pfrommer, J.; Schwarze, M.; Dau, H.; Driess, M. *Angew. Chem. Int. Ed.* 2013, *52*, 13206.

[56] Gorlin, Y.; Jaramillo, T. F. *J. Am. Chem. Soc.* 2010, *132*, 13612.

[57] Takashima, T.; Hashimoto, K.; Nakamura, R. *J. Am. Chem. Soc.* 2011, *134*, 1519.

[58] Morita, M.; Iwakura, C.; Tamura, H. *Electrochim. Acta.* 1977, *22*, 325.

[59] Morita, M.; Iwakura, C.; Tamura, H. *Electrochim. Acta.* 1978, *23*, 331.

[60] Takashima, T.; Hashimoto, K.; Nakamura, R. *J. Am. Chem. Soc.* 2012, *134*, 18153.

[61] Post, J. E. *Proc. Natl. Acad. Sci. U.S.A.* 1999, *96*, 3447.

[62] Mohammad, A. M.; Awad, M. I.; El-Deab, M. S.; Okajima, T.; Ohsaka, T. *Electrochim. Acta.* 2008, *53*, 4351.

[63] Magnuson, A.; Frapart, Y.; Abrahamsson, M.; Horner, O.; Å kermark, B.;

Sun, L.; Girerd, J.-J.; Hammarström, L.; Styring, S. *J. Am. Chem. Soc.* 1998, *121*, 89.

[64] Doeff, M. M.; Anapolsky, A.; Edman, L.; Richardson, T. J.; De Jonghe, L. C. *J. Electrochem. Soc.* 2001, *148*, A230.

[65] Bediako, D. K.; Surendranath, Y.; Nocera, D. G. *J. Am. Chem. Soc.* 2013, *135*, 3662.

[66] Padhi, A. K.; Nanjundaswamy, K. S.; Goodenough, J. B. *J. Electrochem. Soc.* 1997, *144*, 1188.

[67] Harrison, W. T. A.; Gier, T. E.; Stucky, G. D. *J. Mater. Chem.* 1991, *1*, 153.

[68] Kang, B.; Ceder, G. *Nature* 2009, *458*, 190.

[69] Zanazzi, P. F.; Leavens, P. B.; White, J. S. *Am. Mineral.* 1986, *71*, 1224.

[70] Robinson, D. M.; Go, Y. B.; Mui, M.; Gardner, G.; Zhang, Z.; Mastrogiovanni, D.; Garfunkel, E.; Li, J.; Greenblatt, M.; Dismukes, G. C. *J. Am. Chem. Soc.* 2013, *135*, 3494.

[71] Tamaru, M.; Barpanda, P.; Yamada, Y.; Nishimura, S.-i.; Yamada, A. *J. Mater. Chem.* 2012, *22*, 24526.

[72] Li, G.; Azuma, H.; Tohda , M. *Electrochem. Solid-State Lett.* 2002, *5*, A135.

[73] Liu, W.; Farrington, G. C.; Chaput, F.; Dunn, B. *J. Electrochem. Soc.* 1996, *143*, 879.

[74] Kim, H.; Lee, S.; Park, Y.-U.; Kim, H.; Kim, J.; Jeon, S.; Kang, K. *Chem.*

Mater. 2011, *23*, 3930.

[75] Tamaru, M.; Chung, S. C.; Shimizu, D.; Nishimura, S.-i.; Yamada, A. *Chem. Mater.* 2013, *25*, 2538.

[76] Barpanda, P.; Nishimura, S.-i.; Yamada, A. *Adv. Energy Mater.* 2012, *2*, 841.

[77] Adam, L.; Guesdon, A.; Raveau, B. *J. Solid State Chem.* 2008, *181*, 3110.

[78] Sun, Y. K.; Jeon, Y. S.; Leeb, H. J. *Electrochem. Solid-State Lett.* 2000, *3*, 7.

[79] Wizansky, A. R.; Rauch, P. E.; Disalvo, F. J. *J. Solid State Chem.* 1989, *81*, 203.

[80] Suntivich, J.; Gasteiger, H. A.; Yabuuchi, N.; Shao-Horn, Y. *J. Electrochem. Soc.* 2010, *157*, B1263.

[81] Lee, S. W.; Carlton, C.; Risch, M.; Surendranath, Y.; Chen, S.; Furutsuki, S.; Yamada, A.; Nocera, D. G.; Shao-Horn, Y. *J. Am. Chem. Soc.* 2012, *134*, 16959.

[82] Campbell, K. A.; Lashley, M. R.; Wyatt, J. K.; Nantz, M. H.; Britt, R. D. *J. Am. Chem. Soc.* 2001, *123*, 5710.

[83] Klewicki, J. K.; Morgan, J. J. *Environ. Sci. Technol.* 1998, *32*, 2916.

[84] McAlpin, J. G.; Surendranath, Y.; Dincă, M.; Stich, T. A.; Stoian, S. A.; Casey, W. H.; Nocera, D. G.; Britt, R. D. *J. Am. Chem. Soc.* 2010, *132*, 6882.

[85] Oxford, G. A. E.; Chaka, A. M. *J. Phys. Chem. C.* 2012, *116*, 11589.

[86] Grimaud, A.; May, K. J.; Carlton, C. E.; Lee, Y.-L.; Risch, M.; Hong, W.

T.; Zhou, J.; Shao-Horn, Y. *Nat. Commun.* 2013, *4*.

[87] Risch, M.; Grimaud, A.; May, K. J.; Stoerzinger, K. A.; Chen, T. J.; Mansour, A. N.; Shao-Horn, Y. *J. Phys. Chem. C* 2013, *117*, 8628.

[88] Grimaud, A.; Carlton, C. E.; Risch, M.; Hong, W. T.; May, K. J.; Shao-Horn, Y. *J. Phys. Chem. C* 2013, *117*, 25926.

[89] Zhou, H.; Upreti, S.; Chernova, N. A.; Hautier, G.; Ceder, G.; Whittingham, M. S. *Chem. Mater.* 2010, 23, 293.

[90] Tasker, P. *J. Phys. C: Solid State Phys.* 1979, 12, 4977.

[91] Subbaraman, R.; Tripkovic, D.; Chang, K.-C.; Strmcnik, D.; Paulikas, A. P.; Hirunsit, P.; Chan, M.; Greeley, J.; Stamenkovic, V.; Markovic, N. M. *Nat. Mater.* 2012, *11*, 550.

[92] Chakhalian, J.; Millis, A. J.; Rondinelli, J. *Nat. Mater.* 2012, *11*, 92.

[93] Maitra, U.; Naidu, B.; Govindaraj, A.; Rao, C. *Proc. Natl. Acad. Sci. U.S.A.* 2013, *110*, 11704.

[94] Baur, W. *Acta Crystallogr.* 1974, *B30*, 1195.

[95] Aakesson, R.; Pettersson, L. G. M.; Sandstroem, M.; Wahlgren, U. *J. Am. Chem. Soc.* 1994, *116*, 8705.

국 문 초 록

물로부터 산소와 수소를 얻는 물 분해 반응은 태양에너지를 화학에너지로 변환하는 새로운 친환경 에너지 시스템으로 각광받고 있다. 산소 발생 반응은 전체 물 분해 반응의 속도 결정 단계로 작용하고 있기 때문에, 효율적인 산소 발생 촉매의 개발의 중요성이 대두되고 있다. 흥미롭게도, 식물 내 광합성계 II에 있는 Mn_4CaO_5 클러스터는 인공적으로 만들어진 그 어떠한 산소 발생 촉매들에 비해 높은 산소 발생 촉매 효율을 보이고 있다. 따라서 본 연구에서는 자연계의 Mn 기반의 클러스터의 구조와 산화가수에서 영감을 얻어 중성조건 하에서 산소 발생 촉매 특성이 뛰어난 새로운 Mn 기반의 인공광합성 촉매들을 개발하고, Mn 의 구조와 산화가수가 촉매 특성에 미치는 영향을 평가하였다.

첫째로 Mn 원자들이 비대칭적으로 배열 되어 있는 Mn_4CaO_5 클러스터의 구조적인 특징에서 영감을 받아, Mn 원자들이 포스페이트 (PO_4) 그룹에 의해서 비대칭적으로 연결되어있는 새로운 $Mn_3(PO_4)_2$-$3H_2O$ 결정을 합성하였고, 이의 결정구조를 제1원리 계산과, Rietveld 분석을 통해 새롭게 밝혀내었다. Cyclic Voltammetry(CV) analysis와 Gas Chromatography(GC) 분석을 통해 새롭게 만든 $Mn_3(PO_4)_2$-$3H_2O$가 기존에 보고되었던 Mn 기반의 옥사이드 촉매에 비해서 높은 산소발생 특성을 나타내는 것을 확인하였다. 만들어진 $Mn_3(PO_4)_2$-$3H_2O$의 높은 촉매특성의 원인을 파악하기 위하여, Electro paramagnetic Resonance (EPR) 실험과 제1원리 계산 (DFT)를 결합하여 확인한 결과, 중성조건에서도 Mn(III) 중간체가 Mn원자들의 비대칭성으로 인해 안정적으로 존재하는 것을 확인하였다.

두번째로, Mn_4CaO_5 클러스터의 전자배치에서 영감을 받아, Mn의 산화가수가 어떻게 인공광합성 촉매특성에 영향을 주는지 평가해보았다. 이를 위한 Model System으로써 새로운 Li-battery

음극물질인 $Li_2MnP_2O_7$에서 Li을 순차적으로 제거하여 전체적인 구조는 동일하나 Mn의 산화상태가 다른 $Li_2MnP_2O_7$, $Li_{1.7}MnP_2O_7$, $Li_{1.5}MnP_2O_7$, $Li_1MnP_2O_7$ 을 합성하였다. Cyclic Voltammetry(CV) analysis을 통해서 Mn의 산화가수가 2가에서 3가로 변화함에 따라 촉매특성이 점진적으로 향상되는 것을 확인하였다. Mn의 산화가수가 촉매특성에 미치는 영향을 이론적으로 알아보기 위하여, 제1원리 계산을 실행한 결과 Mn의 산화가수가 3가에 가까워질수록 Mn의 Distortion index가 증가하여 Mn(III) 중간체가 안정적으로 존재할 수 있음을 확인 할 수 있었다.

종합적으로 본 연구에서는 $Mn_3(PO_4)_2$-$3H_2O$와 $Li_{2-x}MnP_2O_7$ 물질의 촉매 특성을 실험적으로 평가하였고 그 특성을 제 1원리 계산을 통해서 분석함으로써, Mn의 구조와 산화가수가 산소 발생 촉매 특성에 미치는 영향을 각각 밝혀낼 수 있었다. 이 연구 결과를 기반으로 Mn의 산화가수와 구조를 조절함으로써 자연계의 Mn_4CaO_5 클러스터와 필적할 산소 발생 촉매 특성을 나타낼 수 있는 새로운 Mn 기반의 촉매의 개발이 가능해질 것으로 생각된다.

주요어: 물 분해, 산소 발생 촉매, 망간 포스페이트, 리튬 망간 파이로포스페이트, 중성, 망간 산화수 및 구조

학 번: 2012 - 20600

감사의 글

2 년간의 행복했던 석사과정을 마치며, 부족한 저를 새로운 길로 이끌어주시고 좋은 방향으로 성장시켜주신 많은 분들께 감사의 글을 올립니다.

가장 먼저, 학부시절부터 석사과정까지 항상 큰 관심과 사랑으로 저를 지도해주신 남기태교수님께 진심으로 감사 드립니다. 교수님과 함께 연구들을 진행하면서, 연구의 진정한 기쁨을 알게 되었고, 평생 연구를 해야겠다는 확신을 하게 되었습니다. 교수님께 지도를 받았던 것은 제 인생에서 가장 행복한 일 중에 하나였다고 자신 있게 말할 수 있습니다. 교수님께서 늘 말씀해주셨듯이, 'Aggressive in a good way' 라는 마음가짐으로 앞으로의 연구 활동에서도 창의적이고 적극적인 모습으로 임할 것입니다. 이를 통하여, 교수님께 항상 자랑스러운 제자로 성장하도록 꾸준히 노력하겠습니다.

또한 저에게 애정을 보여주시고, 공동연구를 통해서 제 주제를 훨씬 더 풍부하고, 심도 깊게 발전시켜 주신 한승우 교수님, 강기석 교수님께 진심으로 감사 드립니다. 두 교수님께서 부족한 저를 도와주시지 않으셨다면, 이렇게 좋은 석사주제로 졸업을 할 수 없었을 것 입니다. 제가 모르는 것이 많아서, 교수님들께 이것저것 질문을 드릴 때마다 항상 웃어주시면서 친절하게 저를 지도해주셨던 것이 기억납니다. 두 교수님의 사랑을 통해

석사기간이 행복했습니다. 뿐만 아니라, 이러한 연구 끝에 진심 어린 조언과 사랑으로 저의 학위논문을 심사해주셔서 정말로 감사 드립니다.

또한 제가 학부 1학년때부터 저에게 항상 용기를 북돋아 주시고, 인생에 있어서 중요한 조언을 해주시는 주영창 교수님께 항상 감사 드립니다. 비록 제가 이제는 학교를 떠나게 되지만, 가장 저를 오랫동안 봐오신 교수님이시기에, 앞으로도 교수님께 자주 찾아 뵈며 많은 조언을 구하고 싶습니다. 특히나 교수님께서 보여주신 인자함과 따스하신 성품은 제가 앞으로 살아갈 때 꼭 본받아야 할 점이라 생각합니다.

그리고 처음으로 재료공학부에 입학하여 연구실 생활을 통해서 연구에 대한 흥미를 일깨워주시고, 항상 사랑으로 이끌어주신 황철성 교수님께 감사의 말씀 올립니다. 교수님의 지도를 통해서 재료공학에 대한 자부심과 확신을 갖게 되었습니다. 앞으로 교수님처럼 멋진 연구를 할 수 있는 박지민이 되도록 항상 최선을 다하겠습니다.

또한 이번 연구에 중요한 도움을 주시고, 항상 좋은 조언을 해주신 장호원 교수님께 감사 드립니다. 뿐만 아니라, 학부시절에 진로에 대해서 고민을 하고 있을 때 귀한 시간을 내주시고, 좋은 방향으로 저를 이끌어주신 김기범 교수님과 박은수 교수님께 감사 드립니다.

처음 과학고등학교 재학 시에 고등학생 신분임에도 불구하고, 직접 실험실에서 진행되고 있는 프로젝트에 저를 참여시켜 주시며, 연구의 재미와 과학에 대한 흥미를 일깨워주신 서울대학교

화학생물학부의 이종협 교수님께 감사 드립니다. 또한, 제가 학계에서의 연구 경험 이외에도 직접 병원 연구실에서 환자에게 쓰이는 약물을 개발할 수 있는 귀한 기회를 주셨던 분당 서울대학교 병원 김상은 교수님께도 감사의 말씀 올립니다. 그리고 이번 연구에 있어서 큰 역할을 맡아주신 EPR 분석의 김선희 박사님께 감사의 말씀 올립니다.

또한 석사기간을 시작하면서 앞으로의 연구자로써의 삶에 있어서 저를 아들같이 생각해주시고 진심 어린 조언과 사랑을 보여주신 KIST의 박상환교수님과, 오상록교수님께 감사합니다. 항상 말씀해주셨듯이, 장기적인 안목을 갖고 연구와 그 외적인 것의 균형을 맞추며 남을 위하는 연구자가 되겠습니다. 또한, 제가 졸업하고 입사하게 될 KIST 내 의공학 연구소 생체재료 연구단의 석현광 교수님, 이관희 박사님, 김유찬 박사님 그리고 많은 선책임 박사님들께 진심으로 감사의 말씀을 올립니다. 학생신분에서 벗어나 새로운 곳으로 향하기 위한 준비를 하던 과정 속에서, 박사님들께서 적극적으로 저에게 관심을 보여주시고 도와주신 것이 기억납니다. 6년동안 있었던 학교를 벗어나, KIST라는 새로운 환경으로 간다는 사실에 설레며, 세계적인 연구를 통해 한 단계 크게 발전할 저의 모습 또한 기대됩니다.

항상 웃으면서 행복한 연구실 생활을 할 수 있게 도와주신 우리 실험실 분들 너무나도 감사합니다. 졸업하시고 새로운 인생을 시작하신 태열이형, 정호형 항상 연구를 진행하면서 어려운 문제점이 생기면 형들께 여쭤보며 많이 배웠습니다. 뿐만 아니라, 실험 이외에 사적으로 많이 용기도 북돋아주시고, 응원해주셔서

너무나 감사 드리며, 앞으로 항상 행복하시고 좋은 일들만 가득하길 바래요. 그리고 저희 연구실의 원년멤버이자 너무 너무 성품이 좋으신 욱형. 힘든 일 있을 때마다 형께 많이 고민 상담도 많이 드리고 의지했던 것 같아요. 앞으로도 형수님이랑 행복한 결혼생활 이어가시고 연구도 대성하시길 기원해요! 그리고 제 옆자리에서 절 잘 이끌어주셨던 용선이형! 항상 밝은 미소로 사람들을 편하게 해주시고, 연구도 잘하셔서 제가 옆에서 많이 배웠어요. 나이 차이가 많이 났는데 항상 편하게 형께 말씀도 드릴 수 있었어요. 앞으로 행복한 일만 가득하시길 기도할게요. 그리고 저희 연구실의 시니어이신 해린 누나 혜은 누나! 누나들이 있어 저희 연구실이 더욱 좋은 방향으로 발전해나가는 것 같아요. 처음 인턴 때부터 저를 챙겨주셨던 해린 누나, 이번 박사 졸업 이후에도 지금처럼 좋은 논문들 많이 쓰시고 대성하시길 바랄게요! 혜은 누나 2014년은 더욱 행복한 일만 가득하시길 바라며, 졸업 전에 노래방 한번 더 같이 가요 ^^

또한 저희 방에서 굳은 일을 도맡아 하시는 희윤이형 항상 그 노력에 감사한 마음이 있어요. 형의 기발한 아이디어를 통해서 2014년 한해 최고의 해가 되시길 기원해요! 그리고 항상 웃으면서 사람들 기분을 좋게 해주셨던 선애 누나! 준비하고 계시는 큰 꿈에 좋은 일들이 누나 앞에 다가올 거라 믿어 의심치 않아요! 그리고 진연이! 앞으로 KIST 가서도 계속 지금처럼 잘 지내고 앞으로도 긍정적인 마음과 함께 즐거운 생활을 하길 바랄게! And Gajendra! I wish you good luck on your research! 그리고 재훈, 효용, 영혜, 성은누나, 승학이! 그 동안 연구뿐만

아니라 사적으로 많이 만나고 수다 떨면서 연구실 생활을 행복하게 할 수 있었어! 재훈아 너는 마음이 따뜻하고 남을 배려할 줄 아는 아이 같아. 앞으로도 그런 좋은 성품과 함께 그리고 타이로신과 함께 대성할 거라고 믿어 의심치 않아. 효용아 처음 효용씨 하고 어색하게 불렀던 게 엊그제 같은데 정말 많이 가까워졌다. 나보다 일년후배인데도 연구도 잘하고 마음도 깊어서 연구뿐만 아니라 그 외적인 부분에서도 많은 이야기를 나누었던 것 같아, KIST 가더라도 계속 연락할게! 그리고 어린데도 리더십 있고 많은 사람을 아우르는 능력을 가진 영혜야! 앞으로도 많은 사람들을 챙겨주고 최고의 연구를 하는 너의 모습 기대할게~ 남들을 기분 좋게 해주는 성은누나! 앞으로도 좋은 연구하시길 바라고 KIST 실험하러 오실 때 연락주세요! 한 때 우리방 막내였고, 고생 많았던 승학이. 6개월 같이 있었는데, 학회도 같이 가고 이야기도 많이 정말 많이 했네. 진심으로 앞으로 하는 일들 잘되길 바라고, 졸업 전에 많이 보자 ^^

그리고 우리방 신입들, 혜경이, 유경이, 동혁이, 우제, 윤영이! 졸업이랑 겹쳐서 많은 이야기들을 못 나눠서 미안해요. 최고의 연구실에 온걸 환영하고 앞으로의 연구도 잘 되길 바랄게요!

그리고 내가 사랑하는 중현이형, 아림누나, 기동이. 중현이형! 앙짱님! 연구실 들어와서 형과 보낸 시간이 가장 많은 것 같아요 ^^ 형이랑 2년전 겨울에 관악산을 보면서 얘기하던 게 엊그제 같은데 벌써 이별이라니 너무 아쉽네요. 형한테 정말로 의지 많이 했던 거 알죠? 많이 보고 싶을 거에요, 우리 자주 봐요. 그리고 아림추! 누나가 있어서 진짜 연구실 생활이 재미 있었어요.

신입생환영회, 엠티, 잦은 사적인 만남 진짜 많은 기억을 같이 공유했잖아요. 비록 누나랑 저랑 서로 떨어져있지만, 자주 만나고 조만간 양복도 기대할게요 ^^ 그리고 기동이! 물 분해부터 MEIS 까지 모든 연구를 함께하며 가장 가깝게 지낸 기동아~ 너는 항상 착하고 남의 말을 잘 들어주는 성격이라서 모두가 너를 좋아하는 것 같아. 힘든 일 있을 때마다 서로 고민 털어놓고 기쁜 일은 함께해서 너무나 행복했어. 앞으로도 연구 그리고 그 외적으로도 계속 같이하면서 지내자 ^^

마지막으로 사수 경석이형. 형이랑 이년간 많은 실험도 같이 하고 이야기도 해서 행복했어요. 형한테 많이 의지한 것 같아 항상 죄송하면서 또한 감사해요. 형이 준비하시고 있는 많은 일들 다 잘 풀리시길 기도하고, 앞으로도 좋은 주제가 있으면 같이 연구했으면 좋겠어요 ^^

또한 코웍을 통해서 알게 된 주희 누나, 형섭이형, 인철이형, 병주, 종순이형 다들 감사합니다. 제가 그 동안 많은 걸 부탁드려도 친절하게 설명하고 도와주셔서 너무나 감사 드립니다.

그리고 같이 일하면서 서로 많이 의지하고 많은 시간을 보낸 현아야~ 항상 고맙고 앞으로의 대학원 생활도 밝은 성격과 함께 잘 보낼 거 라고 믿어. 앞으로 학교 자주 놀러 올게.

그 이외에 학부시절부터 친하게 지내며 진지한 진로에 대한 고민을 공유하고, 많은 생활을 함께한 교진이, 용진이, 광훈이, 홍민이, 동하, 경섭이, 구택이형 고맙고, 고등학교 때부터 8년 넘게 단절 없이 내 곁을 지켜준 태권이, 종수, 종하, 예근이, 민성이 너무 고마워.

또한 제가 대학원생활을 할 수 있도록 끝없는 믿음을 보내주신 관정 이종환 교육재단 이종환 이사장님께 감사 드리며, 지난 이년간 관정인들과 소통하며 서로의 기쁨과 아픔을 나눌 수 있어서 행복했습니다.

마지막으로 저에게 무한한 신뢰와 사랑을 아낌없이 주시는 우리 가족! 아버지, 어머니, 누나, 매형! 언제나 내편에서 같이 기뻐해주고, 힘든 일은 진지하게 고민해주시는 우리 가족 너무나 사랑합니다. 한 걸음씩 성장하는 저에게 큰 힘을 항상 보내주셔서 너무나 감사하며, 이제는 한층 더 성숙하고 의젓하며, 말씀하신 대로 '남을 위한 삶'을 살기 위해서 더욱 노력하겠습니다. 정말 많이 사랑하고 또 감사합니다.

긴 감사의 글에서 알 수 있듯이, 저는 부족함에도 불구하고 많은 사람들의 사랑을 받고 성장해왔습니다. 앞으로는 받은 사랑과 관심을 더욱 감사히 여기며, 저 역시 남들에게 더욱 받은 사랑을 더욱 베풀도록 노력하겠습니다. 잔잔한 파도는 훌륭한 뱃사공을 만들 수 없다는 말 같이, 끝없는 역경을 도전적으로 임하여 모든 분들의 사랑에 보답할 수 있는, 세상에 기여하는 박지민이 될 것을 약속 드립니다. 다시 한번 모든 분들께 감사 드립니다.